Reaction Chemistry & Engineering

Kinetic and Mechanistic Studies of Cyclohexane Oxidation with *tert*-Butyl hydroperoxide over M-N_4 Catalysts

Journal:	*Reaction Chemistry & Engineering*
Manuscript ID	RE-ART-01-2025-000031.R2
Article Type:	Paper
Date Submitted by the Author:	09-Apr-2025

Complete List of Authors:	Iaia, Ethan; The University of Alabama, Miller, Miles; The University of Alabama, Department of Chemical and Biological Engineering Soyemi, Ademola; The University of Alabama, Department of Chemical and Biological Engineering Bakker, Martin; The University of Alabama, Department of Chemistry and Biochemistry Szilvasi, Tibor; The University of Alabama, Chemical and Biological Engineering Harris, James; The University of Alabama, Chemical and Biological Engineering

Kinetic and Mechanistic Studies of Cyclohexane Oxidation with *tert*-Butyl hydroperoxide over M-N_4 Catalysts

Ethan P. Iaia,[1] Miles G. Miller,[1] Ademola Soyemi,[1] Martin G. Bakker,[2] Tibor Szilvási,[1] James W. Harris[1*]

1. Department of Chemical and Biological Engineering, The University of Alabama, Tuscaloosa, AL, 35487
2. Department of Chemistry and Biochemistry, The University of Alabama, Tuscaloosa, AL, 35487

Abstract

Oxidation of cyclohexane with *tert*-Butyl hydroperoxide (TBHP) is a common probe reaction for molecular complexes, though the kinetics of this reaction are seldom reported. Here, we synthesize metal- nitrogen-doped carbons (M-N-Cs) and a series of zeolite-encapsulated metal phthalocyanine (MPC) catalysts and compare their reactivity in cyclohexane oxidation with TBHP. These materials all have primary binding sites that include square planar metals bound to four nitrogen atoms (M-N_4 sites). We measure the apparent activation energy for this reaction, and compare the reactivity of M-N-C and MPC catalysts with varied metal central atoms (M = Fe, Mn, Co, Cu, Cr, Ni), of which Fe-containing catalysts are the most reactive. Fe-N-C catalysts are more stable with reuse than are FePC catalysts. Apparent reaction orders are less than one for both reactants, suggesting a surface mediated reaction, Cyclohexanol and cyclohexanone form in parallel at short reaction times, while cyclohexanol further reacts to cyclohexanone at longer reaction times. DFT calculations show that the reaction may follow a radical-mediated Eley-Rideal mechanism that is primarily mediated via *tert*-butoxy radicals formed at the metal site. Microkinetic modeling of the proposed mechanism reproduces experimental trends in production rates and selectivity of the main reaction products without performing any parameter estimation. This study demonstrates that M-N-C and MPC catalysts perform cyclohexane oxidation with TBHP with similar per metal-atom initial rates. These results will enable judicious use of cyclohexane oxidation with TBHP as a probe reaction to compare reactivity of catalysts with M-N_4 active sites.

Keywords: oxidation, doped carbon, phthalocyanine, cyclohexane, KA oil, zeolite, catalyst
*corresponding author, e-mail: james.harris@eng.ua.edu

1. Introduction

Nylon 6,6 is a widely used polymer in the textile industry, that is synthesized through a condensation polymerization of adipic acid and hexamethylenediamine.[1, 2] Adipic acid is synthesized industrially by the oxidation of a mixture of cyclohexanol and cyclohexanone, which is known as "KA oil".[3] Current industrial production of KA oil requires harsh reaction conditions (e.g., 438 K, 1.5 MPa), and must be run at low cyclohexane conversions (10-12%) to maintain selectivity.[4] Additionally, cobalt naphthenate homogeneous catalysts used in this process are harmful to humans if they are exposed, and can be difficult to separate from the product solution.[5] Development of new heterogeneous catalysts can offer solutions to some of these limitations, though this study will focus on comparing kinetic descriptions between different types of catalysts rather than optimizing for industrial purposes.

Square planar Fe complexes, such as metal porphyrins and phthalocyanines (MPC), have been of interest for alkane oxidation due to their similarities to oxygenase enzymes such as cytochrome P-450.[6-9] The Fe-N_4 sites in these complexes also resemble the most reactive sites in metal nitrogen-doped carbons (M-N-C) used in electrochemistry,[10, 11] and more recently in thermal catalysis,[12-15] including cyclohexane oxidation.[16, 17] While M-N-Cs show promise, they are often themselves heterogeneous containing different M-N_x species, complicating the development of structure-function relationships in catalytic systems.[18, 19] Well-defined complexes such as MPC avoid these structural heterogeneities,[20] however they often deactivate in homogeneous catalytic systems with peroxide oxidants.[8, 21, 22] Inclusion within the supercages of faujasite (FAU) zeolites can improve the stability of these catalysts.[8, 22]

MPCs encapsulated within FAU supercages (MPC@FAU) have been investigated for cyclohexane oxidation previously using molecular oxygen,[6] iodosylbenzene,[8, 23] hydrogen peroxide[6] and *tert*-butyl hydroperoxide (TBHP)[8, 23, 24] as oxidants, but few of these studies probe the kinetic pathways that lead to the observed product distributions. Armengol and coworkers[21] compared cyclohexane oxidation rates over CuPC samples using both TBHP and hydrogen peroxide as oxidants, and observed less decomposition of CuPC when using TBHP compared to hydrogen peroxide. Balkus and coworkers[23] studied the room temperature oxidation of cyclohexane with TBHP over RuF_{16}PC@FAU, and measured a turnover frequency (TOF) of 0.04 s^{-1} after 691 ks with 98% selectivity to cyclohexanol. This TOF was ~8× higher than that measured over RuF_{16}PC in the same system, suggesting that the zeolite structure helps to stabilize the MPC in the presence of TBHP,[23, 24] which is known to bleach MPCs.[6, 8, 23] Raja and Ratnasamy[6] studied cyclohexane oxidation over $CuCl_{16}$PC@FAU, $FeCl_{16}$PC@FAU, and $CoCl_{16}$PC@FAU at 343 K using both TBHP and molecular oxygen as oxidants. TOFs measured over $CuCl_{16}$PC@FAU, $FeCl_{16}$PC@FAU, and $CoCl_{16}$PC@FAU were 0.11 s^{-1}, 0.054 s^{-1}, and 0.051 s^{-1} respectively, which were significantly higher than the free MPC complex and ion-exchanged FAU in the same system. Cyclohexane conversion was improved when both TBHP and molecular oxygen were used as oxidants compared to each one separately, suggesting the reaction proceeds through a radical.[6] The radical type mechanism is also suggested by Balkus et al.[23] as no reaction occurred when a radical trap was added. Raja and Ratnasamy[6] also investigated the impact of different solvents, and found that while reaction in acetonitrile had slightly lower TOF than pyridine and acetic acid, formation of side products was limited. Parton and coworkers[8] achieved 95% selectivity to KA oil at 298 K using TBHP as the oxidant over FePC@FAU. While other studies[6, 24, 25] have suggested that this reaction proceeds through a series pathway where cyclohexane is oxidized to cyclohexanol, which is further oxidized to cyclohexanone, Parton et al.[8] suggested that decreases in cyclohexanol concentration over time may be due to competitive adsorption, and that cyclohexanone could be

produced through a parallel pathway. Another study found that depositing FePC on carbon black (CB) showed increased cyclohexane oxidation activity compared to FePC@FAU due to the hydrophobic nature of the carbon support which leads to a higher cyclohexane to TBHP ratio near the active centers compared to the hydrophilic FAU which favors adsorption of TBHP and polar solvents.[26] FePC/CB suffered from destruction of FePC by TBHP due to leaching into solution.[26] Anchoring a Fe-N_4 site in a carbon framework (Fe-N-C) may offer the benefits of the hydrophobic carbon while protecting active sites from TBHP. Direct comparisons of MPC@FAU to M-N-C materials in the same system, as well as density functional theory (DFT) calculations may offer more insights into the mechanism of this process.

Here we report synthesis and characterization of a series of heterogeneous metal-containing catalysts (M = Fe, Mn, Co, Cu, Cr, Ni), specifically MPCs encapsulated (MPC@FAU) and deposited (MPC/FAU) on FAU zeolites, as well as M-N-Cs. These samples were tested for the oxidation of cyclohexane with TBHP over a temperature range of 298-333 K. Kinetic trends across varied metal centers are reported. Conversions of cyclohexane are intentionally kept low to simplify kinetic measurements and comparisons between M-N-C and MPC@FAU catalysts. These kinetic measurements may aid in optimization for industrial purposes in the future, but that is not the focus of this study. Comparisons to computational studies provide insight into the observed product distributions with time.

2. Experimental methods

2.1 Catalyst synthesis

2.1.1 Synthesis of Na/FAU

As prepared FAU zeolites with no MPC will be denoted as "Na/FAU". Na/FAU samples were synthesized according to a modified procedure from literature.[27, 28] The following ingredients were added to a 60 cm^3 perfluoroalkoxy alkane (PFA) jar (Savillex): 21.14 g Millipore water (18.2 MΩ), 0.699 g aluminum hydroxide (Sigma Aldrich, 51 wt% Al_2O_3), 2.31 g NaOH (Sigma Aldrich, 97%), and seven g of LUDOX HS-30 colloidal silica (Sigma Aldrich, 30 wt%). A 30 mm stir bar (VWR) was added, and the mixture was stirred at ambient temperature for 86 ks while capped. The stirred mixture was then transferred to a 45 cm^3 acid digestion vessel (Parr Instrument Co.) with a polytetrafluoroethylene (PTFE) liner. The vessel was heated at 358 K for 130 ks in a static oven (VWR). The resulting solids were then removed from the vessel and washed five times with Millipore water (~40 g per sample per wash) via vortex mixing (VWR), and separated by centrifugation (Thermo Scientific, Sorvall ST1 Plus, 133 Hz for 360 s, 50 cm^3 centrifuge tubes). Samples were then dried overnight in a gravimetric oven at 363 K, then calcined at 823 K for 36 ks in a muffle furnace (Nabertherm, 0.017 K s^{-1} ramp, 1.67 cm^3 s^{-1} of house air), to yield as prepared Na/FAU samples.

2.1.2 Synthesis of MPC@FAU

MPC@FAU samples were synthesized with the same procedure outlined above for Na/FAU, but 0.075 g of the desired MPC was added to the PFA jar before stirring. MPCs used include $CuCl_{16}PC$ (Sigma Aldrich, 100%), $CrCl_{16}PC$ (Porphychem, >95%), $FeCl_{16}PC$ (Porphychem, >95%), $MnCl_{16}PC$ (Porphychem, >95%), $NiCl_{16}PC$ (Porphychem, >95%), $ZnCl_{16}PC$ (Porphychem, >95%), $ZnF_{16}PC$ (Sigma Aldrich, 90%). These samples were not calcined like Na/FAU samples due to the thermal stability limits of the MPCs at 823 K. "Unwashed" MPC@FAU samples were then washed using a Soxhlet extractor (Chemglass, CG-1368-02). 0.400 g of sample were added to a glass fiber thimble (GE Life Sciences, 0.8 μm pore openings), and this thimble was

subsequently placed inside a glass thimble (Chemglass, 60 μm pore openings), and then placed in the middle piece of the Soxhlet extractor. The round bottom flask (RBF) was filled with 200 cm^3 of the desired solvent and placed in an oil bath. The middle piece of the Soxhlet extractor was then attached to the RBF with high vacuum grease (Dow Corning) between the joints. The condenser was attached to the top part of the middle piece in a similar way, and cooled using ambient temperature tap water. Each sample was consecutively washed with a series of three solvents in this order: 86 ks in acetone (VWR, 99.5%) heated to 353 K, 86 ks in pyridine (Beantown Chemical, 99%) heated to 433 K, and 86 ks in acetonitrile (VWR, ≥ 99.5%) heated to 393 K, for a total of 259 ks. The samples were then dried overnight under vacuum (Thermo Scientific Lindberg Blue M, ~10 Torr vacuum) at 363 K to yield "washed" samples, denoted as "MPC@FAU".

2.1.3 Synthesis of MPC/FAU

To deposit MPCs on the external surfaces of Na/FAU crystallites, the following ingredients were added to a 250 cm^3 PFA jar: 0.5 g of calcined Na/FAU made in house, 200 cm^3 of acetone (VWR, 99.5%), and the desired mass of MPC. The mixture was stirred with a 30 mm stir bar (VWR) uncapped in a fume hood at ambient temperature to evaporate off the acetone. The dried powder was collected and will be denoted "MPC/FAU".

2.1.4 Synthesis of Ni, Fe, Mn-N-C

Fe nitrogen-doped carbon samples were synthesized from metal-doped ZIF-8 based on a reported procedure.[12] For Cu, Ni, and Mn-N-C the procedure was adapted to replace the iron nitrate with the corresponding metal nitrate. For solution 1, 4.76 g of zinc nitrate hexahydrate, 0.215 g of iron nitrate nonahydrate, and 500 cm^3 of methanol (VWR, >99.9%) were added to 750 cm^3 Erlenmeyer flask along with a 30 mm stir bar (VWR). The solution was capped with a rubber septum and stirred for ~0.9 ks to combine. For solution 2, 5.26 g of 2-methylimidazole (Thermo Scientific, 99%) and 200 cm^3 of methanol (VWR, >99.9%) were added to a 250 cm^3 PFA jar with a 30 mm stir bar (VWR) and stirred while capped for ~0.9 ks to combine. Solution 2 was then added slowly to solution 1, and stirred while capped for 86 ks at 333 K. The resulting solids were separated by centrifugation (Thermo Scientific, Sorvall ST1 Plus, 133 Hz for 360 s, 50 cm^3 centrifuge tubes) and vortex washed (VWR vortex mixer, ~35 cm^3 solvent per sample per wash) once with methanol (VWR, >99.9%) and three times with ethanol (VWR, 95%), then dried overnight in a gravimetric oven at 363 K; these samples are denoted as "M-ZIF-8". The M-ZIF-8 was then pyrolyzed in a tube furnace (Thermo Scientific, Lindberg Blue M) at 1323 K for 3.6 ks (0.083 K s^{-1} ramp) to yield "M-N-C".

2.1.5 Synthesis of Cu-N-C

Cu-N-C was synthesized according to a reported procedure.[29] For solution A, 0.0209 g of copper nitrate trihydrate and 0.1915 g of zinc nitrate hexahydrate were dissolved in 10 cm^3 of methanol (VWR, >99.9%). In a separate solution B, 1.64 g of 2-methylimidazole (Thermo Scientific, 99%) was dissolved in 40 cm^3 of methanol. Solution A was injected into solution B and then sonicated for 1.8 ks. The sonicated mixture was then transferred to a 125 cm^3 acid digestion vessel (Parr Instrument Co.) with a polytetrafluoroethylene (PTFE) liner. The vessel was heated at 393 K for 86 ks in a static oven (VWR). The resulting solids were then removed from the vessel and washed three times with methanol (~40 g per g sample) via vortex mixing (VWR), and separated by centrifugation (Thermo Scientific, Sorvall ST1 Plus, 133 Hz for 360 s, 50 cm^3 centrifuge tubes). Samples were then dried overnight in a gravimetric oven at 363 K. Once dry, samples were

pyrolyzed in a tube furnace (Thermo Scientific, Lindberg Blue M) at 1173 K for 3.6 ks (0.083 K s^{-1} ramp) to yield Cu-N-C.

2.1.6 Synthesis of Co-N-C

Co-N-C was synthesized by the impregnation of carbon black pearls and subsequent high-temperature pyrolysis according to a reported procedure.[30] For solution 1, 0.5 g of cobalt nitrate hexahydrate (Alfa Aesar, 97.7%) was dissolved in 10 cm^3 of house deionized water. For solution 2, 0.611 g of 1,10 phenanthroline (Sigma Aldrich, ≥ 99%) was dissolved in 15 cm^3 ethanol (Sigma Aldrich, > 99.9%). Solution 1 was added to solution 2 slowly, and the resulting mixture was stirred for 1.2 ks at 353 K. This mixture was then added dropwise to a slurry of carbon black pearls (Cabot) in 0.1 M NaOH (Fischer Scientific, 97.6%) while stirring for 7.2 ks at 353 K. The resulting solids were isolated by vacuum filtration, washed with 2000 cm^3 of house deionized water and dried overnight in a static oven (Fischer Scientific, Isotemp 516G). Once dry, the sample was impregnated with 0.5 g of dicyandiamide (TCI, >98%) in acetone while stirring at 329 K for 43 ks. The solid was then allowed to dry by evaporation to ambient on the benchtop.

The impregnated sample was then thermally treated in a tube furnace (Thermo Scientific, Lindberg Blue M) at 973 K (0.0167 K s^{-1} ramp) for 7.2 ks, in 1.67 cm^3 s^{-1} Helium (Airgas, 99.999%), followed by an acid wash in 250 cm^3 of 1 M HCl (VWR, 36.5-38%) to remove any nanoparticles. The acid-washed sample was then separated by vacuum filtration, washed with 300 cm^3 of house deionized water, and dried overnight in a static oven at 343 K. Once dry, the sample was then thermally treated again in the same tube furnace at 673 K for 7.2 ks (0.0167 K s^{-1} ramp) in a dilute H_2/He mixture (1.67 cm^3 s^{-1} total flow; 101 kPa total pressure; 5 kPa H_2, Airgas, 99.999%; balance He) to yield the final catalyst, which is denoted as "Co-N-C".

2.1.7 Synthesis of Si-xerogel

Si-xerogel was synthesized according to a previously reported procedure.[31] First, concentrated HCl (37%, Sigma Aldrich) was diluted with ultrapure water to make 20 cm^3 of 0.1 M HCl. 2.28 g of this solution, 26.9 g of ultrapure water, and 20.7 g of tetraethyl orthosilicate (TEOS, 98%, Sigma Aldrich) were then added to a 250 cm^3 PFA jar and stirred (30 mm stir bar, VWR) for 7.2 ks. To the now homogenous mixture, 1 M ammonium hydroxide (diluted from 28% NH_4OH, Sigma Aldrich) was added dropwise with a disposable glass pipette until the mixture became a gel-like solid (usually ~68 drops). The stir bar was then removed with a disposable spatula, and the gel was dried overnight at 363 K. The gel was then washed with ultrapure water by vortex mixing (VWR) until the pH of the supernatant after centrifugation remained constant (usually ~5.1). The sample was then calcined in a tube furnace (Thermo Scientific, Lindberg Blue M) at 823 K for 36 ks (0.0167 K s^{-1} ramp, 3 cm^3 s^{-1} air).

2.2 Catalyst characterization

2.2.1 Powder X-ray Diffraction (XRD)

XRD patterns of all hydrothermally synthesized zeolites were collected to confirm the targeted zeolite crystal structure. A Rigaku Smartlab diffractometer equipped with a low background sample holder (Rigaku, 5 mm diameter, 0.2 mm depth), along with the Rigaku Smartlab Studio II software were used to collect patterns between 2-theta angles of 4-50˚ (0.015˚ s^{-1}, 0.1˚ step size).

2.2.2 N_2 Adsorption

A Micromeritics ASAP 2020 was used to measure N_2 adsorption isotherms. Prior to analysis, samples were degassed at 623 K for 32 ks (0.167 K s^{-1} ramp rate). Micropore volumes were obtained by semi-log derivative analysis as described previously.[28, 32] This method was used to calculate all micropore volumes in **Table 1**.

2.2.3 Inductively Coupled Plasma Optical Emission Spectroscopy (ICP-OES)

Elemental compositions of all zeolite and carbon samples were determined by ICP-OES using and Agilent 5800 spectrometer. Zeolite samples were dissolved in 2 cm^3 hydrofluoric acid (HF, VWR, 48-51%) then diluted with 2% nitric acid prior to analysis (*Note: care should be taken when handling concentrated HF!*). Carbon samples were heated at 373 K in nitric acid (70%, VWR) for 7.2 ks, then diluted with Millipore water prior to analysis. Four calibration standards for each element were made to calibrate the instrument, with each solution containing equal concentrations (ppm) of each element in 2 vol% nitric acid (diluted from 70% with ultrapure water, VWR) ranging from 0.1-25 ppm for Fe, Mn, Co, Zn, Si, Al, and Na, with additional standards for Si, Al, and Na with concentrations of 100-500 ppm. Standards were prepared from 1000 ppm stock solutions of each element in 2 vol% nitric acid (Sigma Aldrich, TraceCERT).

2.2.4 Scanning (SEM) and Transmission (TEM) Electron Microscopy

SEM images were collected to give an estimate for the particle sizes of the FAU. Images were collected using a Thermo Scientific Apreo FE-SEM (field emission generator), with spot size of 40 μm and an accelerating voltage of 2 kV.

TEM images were collected using a FEI Tecnai 200i microscope. Samples were dispersed in methanol (VWR, >99.9%) and then sonicated (VWR, 9.5L sonicator) for 3.6 ks. Two drops of this sonicated solution were dropped on a Cu TEM grid (EMS, 50 μm, 200 mesh). The grids were then allowed to dry at ambient conditions for 86 ks prior to use. A voltage of 200 kV was used to collect images. Energy-dispersive X-ray spectroscopy (EDS) was performed at 2048 × 1080 resolution with a dwell time of 50 μs and a total of four frames. EDS signal intensity was enhanced using the pre-filtering option of the Velox TEM software by averaging 20 pixels.

2.2.5 Diffuse Reflectance Ultraviolet-Visible Spectroscopy (DRUV)

Ex situ DRUV spectra were collected using a Shimadzu UV3600 Plus spectrophotometer with a diffuse reflection accessory (Harrick Praying Mantis, DRP-XXX). Scans were collected between 190-900 nm with a one nm resolution at a rate of 1.97 nm s^{-1}. Prior to the first measurement, a 100% reflectance baseline was established using barium sulfate (Sigma Aldrich, 99%). Data were collected in reflectance (R) and converted to Kubelka-Munk absorbance units using eq. 1. [33, 34]

$$F(R) = \frac{(1-R)^2}{2R} \quad (1)$$

2.2.6 X-ray Absorption Spectroscopy (XAS)

X-ray absorption near edge structure (XANES) and extended X-ray absorption fine structure (EXAFS) spectra were collected at the National Synchrotron Light Source (II) at Brookhaven National Laboratory on Inner Shell Spectroscopy beamline 8-ID.[35] Finely ground samples were loaded into 1.8 mm i.d polyimide capillaries (Cole-Parmer) and sealed at both ends with Play-doh (Hasbro). All analyses were performed with the Demeter software suite.[36] EXAFS data of metallic foils were fit to determine amplitude reduction factors (s_0^2) using a crystallographic information

file (CIF) for each metal obtained from the materials project database.[37] s_0^2 values determined from these fits: 0.69 ± 0.07 for Fe, 0.83 ± 0.06 for Cu and 0.77 ± 0.03 for Co.

2.3 Catalytic Trials

Cyclohexane oxidation reactions were carried out in acetonitrile using a borosilicate tube reactor (10 cm length, 2 cm diameter) connected to a 24/40 outer joint sealed with a rubber septum. A 1.05 M stock solution of cyclohexane (Sigma Aldrich, 99.5%) in acetonitrile (VWR, ≥ 99.5%) was prepared by combining 17.7 g cyclohexane and 139 g of acetonitrile in a 250 cm^3 glass media bottle (VWR). To prevent the acetonitrile from evaporating off, this solution was stored in a refrigerator and capped when not in use. First, 0.01-0.02 g of catalyst were weighed and added to the reactor, along with a 9 mm PTFE stir bar (DISC, 6 mm height). Then 4 cm^3 of stock solution was added to the reactor slowly while spinning to catch any catalyst that may be stuck to the sides of the reactor. The reactor was then quickly capped with a rubber septum, and placed in an oil bath heated to the desired temperature, and allowed to stir for 900 s. Then 0.2 cm^3 of the oxidant, *tert*-butyl hydroperoxide (TBHP, Thermo Scientific, ≥ 70% in water) were injected using a syringe. After reaction, the reactor was removed from the oil bath and placed in an ice bath to quench the reaction. The solution was then filtered (VWR, 0.22 μm) and a 1 cm^3 of filtered solution was added to a glass vial along with 0.01 cm^3 of 1-propanol (internal standard, Thermo Scientific, 99.9%). The vial was then vortex mixed to combine, and the solution was analyzed by an Agilent 6890N gas chromatograph (GC) equipped with a flame ionization detector (FID) and a J&W HP-5 GC Column (30 m 19091J-413, Agilent). Conversion was calculated using eq. 2, selectivity using eq. 3, carbon balance was calculated using eq. 4.

$$Conversion = \frac{Cyclohexane_{in} - Cyclohexane_{out}}{Cyclohexane_{in}} = \frac{TBHP_{out} - tBuOH_{out}}{TBHP_{in}} \quad (2)$$

$$selectivity = \frac{mol\ product_A}{total\ mol\ products} \quad (3)$$

$$Carbon\ balance\ (\%) = \frac{Cyclolhexane_{out} + Cyclohexanol_{out} + Cyclohexanone_{out}}{Cyclohexane_{in}} \quad (4)$$

The carbon balance closed to 85 ± 5% for most data reported in this manuscript. **Figure S.1** shows the carbon balance for data reported in **Figure 7.** Species observed by GC-FID include cyclohexane, TBHP, n-propanol, tert-butyl alcohol (tBuOH), cyclohexane, and cyclohexanone. There are no detectable products other than cyclohexanol and cyclohexanone that can account for the missing carbon, even after 14.4 ks of reaction, but it is possible there are some other side products undetectable by GC-FID. Cyclohexyl hydroperoxide (CHHP) is one such product that has been identified by others,[38, 39] and would thermally decompose in the GC inlet[40] to form cyclohexanol and cyclohexanone. It is possible that some CHHP is present in product solutions, but this would be accounted for in the mass balances in **Figure S.1**. Adsorption of cyclohexane to the zeolite can be ignored as stirring different amounts of Na/FAU in 1.05 mol L^{-1} cyclohexane in acetonitrile had no impact on the measured concentration of cyclohexane after stirring for 1.8 ks (**Figure S.2),** but adsorption of products on FAU is a possible explanation for the missing carbon. Other possibilities could include error from weighing out reactants on the balance, error in calculating the GC-FID response factor, and error from one GC injection to another. The initial rate of cyclohexane oxidation was calculated as the sum of the rates of cyclohexanol and cyclohexanone formation, using eqs. 5 and 6 respectively, where m is mass of product in g, MW is the molecular weight in g mol^{-1}, n is the mass of catalyst in g, and t is the batch time in seconds.

$$r_{cyclohexanol} = \frac{m_{cyclohexanol}}{MW_{cyclohexanol} \times n \times t} \quad (5)$$

$$r_{cyclohexanone} = \frac{m_{cyclohexanone}}{MW_{cyclohexanol} \times n \times t} \quad (6)$$

Rates measured over Na/FAU and N-C were subtracted from corresponding samples so that reported rates can be attributed to active metal centers. Due to the limited yield of each M-N-C synthesis, cyclohexane and TBHP reaction order experiments could not all be run with catalysts from the same synthesis batch. To account for batch-to-batch variations, rates for both M-N-C and MPC samples were normalized by the rate measured at the standard condition in each set of experiments, so the rate at standard conditions from the cyclohexane and TBHP reaction order experiments would both be one, prior to regressing to rate expressions using Excel solver.

2.4 Computational Methods

To support experimental findings, electronic structure calculations were performed to give insight into the reaction mechanism for the oxidation cyclohexane to cyclohexanol and cyclohexanone over encapsulated metal phthalocyanines (MPCs) using *tert*-butyl hydroperoxide as an oxidant. In addition, microkinetic modeling (MKM) was performed to elucidate key intermediates and product distributions.

Model Selection for Electronic Structure Calculations

Due to the complexity of zeolite systems (presence of Al atoms, and defects), and the associated computational cost of modeling the zeolite cage along with the PC, careful model selection is very important. Based on our previous study of CO oxidation,[28] it was concluded that it was a reasonable assumption to neglect the zeolite cage during calculations. Our previous calculations also showed that the identity of the peripheral ligands (H, F, or Cl) had minimal effect on the binding energy of adsorbates on the metal active site. Thus, the energetics of cyclohexane oxidation was obtained by modeling the MPC as a single unit in vacuum with hydrogen as the periphery ligand.

Reaction Mechanism Calculations

Geometry optimizations and transition state calculations were performed using the PBE density functional[41] with the def2-SVP basis set[42] and Grimme's Becke-Johnson damped dispersion correction (D3(BJ))[43] in the GAUSSIAN 16 program suite[44] within a spin unrestricted formalism (UDFT). All geometry optimizations and transition state searches were performed using the Berny algorithm as implemented in the GAUSSIAN 16 program suite. In all geometry optimization and transition state calculations, force convergence criteria were set to 4.50 x 10^{-4} Hartree/Bohr (0.023 eV/Å) in maximum force and 3.00 x 10^{-4} Hartree/Bohr (0.015 eV/ Å) in root mean square force (on all atoms). Energy convergence criteria were set to 10^{-6} and 10^{-8} root mean square and maximum change in the density matrix, respectively. Lastly, GAUSSIAN 16 includes atomic displacement convergence criteria for geometry optimization and transition state calculations which were set to 1.80 x 10^{-3} Bohr (9.5 x 10^{-4} Å) in maximum atomic displacement, and 1.20 x 10^{-3} Bohr (6.4 x 10^{-4} Å) in root mean square atomic displacement. Optimized structures were characterized by vibrational analysis performed at the same level of theory at 298 K and 101.3 kPa. Minima were characterized by the absence of imaginary frequencies while transition states were confirmed by the presence of a single imaginary frequency belonging to the reaction

coordinate. For the calculation of single point energies that also incorporated the effects of solvation using the SMD implicit solvation model,[45] calculations were performed at the PBE-D3(BJ)(SMD=Acetonitrile)/def2-TZVPP[42] level of theory using optimized geometries obtained from the previous step.

To obtain Gibbs free energies, the entropic contributions were recalculated using the quasi-harmonic entropic correction scheme of Cramer and Truhlar[46] as implemented in the GoodVibes code (version 3.2)[47] whereby all vibrational frequencies below 100 cm^{-1} are set to 100 cm^{-1}. Gibbs free energies were thus calculated as:

$$G = E_{PBE-D3(BJ)(SMD=Acetonitrile)/def2-TZVPP} + (G_{PBE-D3(BJ)/def2-SVP} - E_{PBE-D3(BJ)/def2-SVP}) \quad (7)$$

Gibbs free energies of reaction (ΔG) were calculated from the algebraic sum of individual free energies of final and initial states as shown below:

$$\Delta G = \sum G_{final} - \sum G_{initial} \quad (8)$$

Similarly, activation Gibbs free energies ($\Delta G^{\ddagger}$) were calculated as the difference between the Gibbs free energy of the transition state (G_{TS}) and that of the initial state ($\sum G_{initial}$) as shown below:

$$\Delta G^{\ddagger} = G_{TS} - \sum G_{initial} \quad (9)$$

Calculation of Rate Constants

Rate constants based on calculated activation Gibbs free energies were calculated using the Eyring-Polányi equation:

$$k = \frac{k_B T}{h} e^{-\frac{\Delta G^{\ddagger 0}}{RT}} \quad (10)$$

where k_B, h, R, and T are the Boltzmann constant, the Planck constant, the ideal gas constant, and the temperature, respectively, while the $\Delta G^{\ddagger 0}$ represents the activation Gibbs free energy corrected to the solution standard state (whereby all solute concentrations equal 1 mol dm^{-3}). As an illustration, $\Delta G^{\ddagger 0}$ equals the DFT calculated activation Gibbs free energy ($\Delta G^{\ddagger}$) for a unimolecular decomposition (i.e., A → B), however $\Delta G^{\ddagger}$ differs by a correction term of -7.93 kJ mol^{-1} (at 298 K and 101.3 kPa) in the case of biomolecular reactions (i.e., A + B → C).[48-51]

For elementary steps where we could not find a barrier, such as steps involving coordination to or dissociation from the metal site of the MPC which depend on diffusion of intermediates, we estimate the Gibbs free energy barrier as a sum of the translational entropy contribution (11 kcal mol^{-1} or 46 kJ mol^{-1})[52] and an estimate of the contribution of diffusion.[53] The diffusion rate was calculated using the Stokes-Einstein eq. with the Smoluchowski formulation[54, 55] as shown in eq. 11.

$$k_D = \frac{8 k_B T}{3\eta} \times 10^3 \times N_A \quad (11)$$

where k_B, is the Boltzmann constant, T it the temperature, ŋ is the viscosity of the solvent (acetonitrile viscosity = 0.346 cP),[56] and N_A is Avogadro's number. Based on the calculated k_D, we then calculate the Gibbs free energy contribution of diffusion to the barrier using eq. 10. While this approach is common in homogeneous catalysis,[53, 55] it neglects the effects of confinement on the diffusion of species within the zeolite. We adopt these approximations for practical reasons as we could not fit to experimental data and to avoid estimating the diffusion rate or translational

entropy via expensive ab initio molecular dynamics. We also estimated the rate of the barrierless steps using collision theory as has been used in previous studies related to zeolite catalysis.[57-59] However, in this case we observed (see Supporting Information for details) only cyclohexanol production (90% selectivity as shown in Figure S.28) and thus the model was inconsistent with experimental results. As we show below, summoning the diffusion and translational entropy contribution to the rate of barrierless steps gives results that are consistent with experimental results.

Microkinetic Modeling

Computational studies of catalytic mechanisms are typically based on the calculation and discussion of intermediate energies and activation barriers. However, this approach may be insufficient in cases where the reaction mechanism is unknown or complex since it is difficult to validate a proposed mechanism without directly comparing to experimental outputs such as rates and product distributions. For example, specific reaction conditions such as initial concentration of reactants or catalyst can greatly influence overall reaction kinetics. Consequently, we performed MKM simulations to connect to experimental measurements.[55]

Having mapped out a network of elementary steps and calculated their rate constants (eq. 10), a system of reaction rate equations can be defined which forms the microkinetic model of the catalytic reaction for all intermediates of the reaction network as follows:

$$\frac{d[I]}{dt} = \sum_i r_{in,i} - \sum_i r_{out,j} = \sum_i k_{in,i}[S_{1,i}][S_{2,i}] - \sum_i k_{out,j}[I][R_j] \quad (12)$$

where $r_{in,i}$ and $r_{out,j}$ stand for the rate of production and rate of consumption of intermediate I, respectively, while while $k_{in,i}$ and $k_{out,j}$ are the corresponding rate constants. $[S_{1,i}]$ and $[S_{2,i}]$ refer to the molar concentrations of the source intermediates of I, while $[R_j]$ represents the concentration of the jth reaction partner of I.

The numerical solution of the system of differential equations above, using experimentally applied initial concentrations as starting conditions, provides the time evolution of the concentration of each component. Crucially, the transient concentrations can be directly obtained by experiments, which allows a simple evaluation of the validity of the proposed mechanism by direct comparison with experiments. In this work, the transient concentrations in the reaction mixture were simulated using the COPASI 4.42 program.[60] The system of reaction rate equations were solved using the LSODA algorithm using a 0.01 s interval. To gain additional insights into the rate/selectivity determining steps, we also performed a sensitivity analysis of the cyclohexanol/cyclohexanone production rate to the elementary steps of the proposed reaction mechanism. Similar to the degree of rate control analysis commonly employed in heterogeneous catalysis[61] to reveal elementary steps that control the overall rate, our sensitivity analysis allows us to probe the effect of elementary steps on each product formation rates. The sensitivity coefficient is defined by the following equation:

$$S_{ij} = \frac{\partial y_i}{\partial p_j} \times \frac{p_j}{y_i} \quad (13)$$

where $\frac{\partial y_i}{\partial p_j}$ represents the partial derivative of output y_i (for example, the cyclohexanol or cyclohexanone production rate) with respect to the parameter p_j (elementary step rate constants), and $\frac{p_j}{y_i}$ is the ratio of the parameter value to the output value that normalizes the sensitivity coefficient to ensure it is dimensionless. Thus, the sensitivity coefficient represents the factor by which y_i changes for a given change in p_j. Sensitivity coefficients are given in **Table S.4.** For this analysis, we ignored reaction steps that were found to be barrierless by DFT. In addition to the

sensitivity analysis, we also performed a numerical degree of selectivity control analysis as shown in equation 14.

$$X_{sc} = \left[\frac{\Delta lnS}{\Delta lnk_i}\right]_{k_{j\neq i}, K_i} \quad (14)$$

S is the ratio of the cyclohexanol production rate to the cyclohexanone production rate, k_i is the rate constant of elementary step i, and K_i is the equilibrium constant of elementary step i which is held constant. For this analysis, we varied k_i by ±0.01.

3. Results and discussion

3.1 Structural characterization of catalysts

Table 1. Structural characterization data for the samples in this study.

Sample	M wt%[a]	Micropore volume[b] / cm^3 g^{-1}	Surface Area[c] / m^2 g^{-1}
Na/FAU	14	0.29	777
$FeCl_{16}PC$/FAU	0.16	0.25	687
$FeCl_{16}PC$@FAU	0.13	0.24	643
Fe-N-C	0.72	0.27	683
$MnCl_{16}PC$/FAU	0.45	*	*
$MnCl_{16}PC$@FAU[d]	0.44	0.24	668
Mn-N-C	0.005	0.23	701
$CoCl_{16}PC$/FAU	0.11	0.22	597
$CoCl_{16}PC$@FAU	0.03	0.24	651
Co-N-C	2.1	0.20	611
CuPC/FAU	0.46	*	*
$CuCl_{16}PC$/FAU	0.08	0.27	748
$CuCl_{16}PC$@FAU	0.02	0.20	542
Cu-N-C	*	0.22	662
$CrCl_{16}PC$/FAU	0.20	*	*
$CrCl_{16}PC$@FAU[d]	0.36	0.32	877
NiPC/FAU	0.16	*	*
Ni-N-C	1.4[e]	0.29	768
N-C	3.7 (Zn)	*	*

[a] Bulk metal composition determined by inductively coupled plasma optical emission spectroscopy (ICP-OES) except where noted.
[b] Micropore volume determined from total N_2 uptake at the end of micropore filling in adsorption isotherms.
[c] Surface areas determined from the BET equation for M-N-C samples and using the BETSI[62] algorithm for zeolite samples
[d] values for these samples were reported previously[28]
[e] Determined by SEM-EDX.
*not measured

The physical characteristics of the various samples were probed using XRD, ICP-OES, and N_2 physisorption. XRD patterns of zeolite and ZIF-8 samples are reported in **Figures S.3 and S.4** respectively, and are consistent with the crystal structures of each material for all samples. After pyrolysis, diffraction peaks for ZIF-8 were absent, and no diffraction patterns representative of

metal nanoparticles or oxides were present, suggesting metal atoms are either isolated, or present as amorphous oligomers undetected by XRD. Bulk metal loadings determined by ICP-OES are reported in **Table 1**. Results for Fe-N-C and Co-N-C were comparable to those measured by other previously using the same synthesis procedure.[12, 30] The measured loading for Mn-N-C was much lower, while Ni-N-C and Cu-N-C were not able to be quantified by ICP-OES. The metal loading of Ni-N-C was instead evaluated using SEM-EDX by taking the average Ni wt% measured in six different areas of the sample (**Figure S.5**, EDX results in **Table S.1**). Cu-N-C could not be evaluated by SEM due to limited sample volume, but XAS results (**Figure S.16**) suggest there is Cu present in the sample. N_2 physisorption determined micropore volumes for MPC@FAU and MPC/FAU samples, which were generally lower than, or consistent with, those typical of Na/FAU zeolites (~0.30 $cm^3\ g^{-1}$), respectively. For M-N-C samples, micropore volumes were similar (~0.27) $cm^3\ g^{-1}$), and BET surface areas (~650 $m^2\ g^{-1}$) were smaller than the unpyrolyzed M-ZIF-8 (~2000 $m^2\ g^{-1}$), consistent with previous reports.[12, 63]

MPC@FAU samples were washed via Soxhlet extraction to remove unencapsulated MPCs as described in **Section 2.1.2**. We have previously shown that this Soxhlet washing procedure removes all MPC from MPC/FAU samples as evidenced by the disappearance of the characteristic Q band from DRUV spectra of washed MPC/FAU samples.[28, 64] DRUV spectra of washed MPC@FAU samples (**Figure S.9**) suggest MPC remains in the sample after washing.

XAS data of MPC and M-N-C samples were used to probe the oxidation state and coordination environment of metal centers in these materials. We have previously reported XANES data for MPC@FAU samples used in this study.[28] The spectra contain pre edge features characteristic of the square planar metal centers in MPC, either in the as prepared state or after heating to 573 K under inert gas flow.[28] EXAFS for each sample was fit in the first shell to a CIF of the given MPC for each MPC@FAU sample obtained from the CCDC database[65, 66] and the parameters obtained from these fits can be found in **Table 2**. R and K space plots can be found in **Section S.6**. These metal-nitrogen coordination numbers of ~4 are consistent with the four metal-nitrogen bonds in metal phthalocyanine, but with the error in these measurements due to the low loadings of the samples, it is possible that the coordination number is actually five, likely due to exposure to air as discussed previously.[28] Since the most reactive sites in M-N-Cs resemble the metal centers in MPC, EXAFS data collected on these samples were also fit in the first shell to a CIF of the corresponding MPC.[65-67] Fe- and Cu-N-C fit to M-N coordination of ~4 consistent with this model,

Table 2. Radial bond distances, coordination numbers, mean squared disorder, and change in adsorption edge energy obtained from EXAFS.

Sample	Path	d / Å	CN	σ^2 / Å^2	ΔE_0 / eV
$FeCl_{16}PC$@FAU	Fe-N_4	1.97 ± 0.07	3.8 ± 3.1	0.004 ± 0.010	-0.4 ± 9.4
$CuCl_{16}PC$@FAU	Cu-N_4	1.97 ± 0.02	4.1 ± 1.2	0.002 ± 0.003	10.1 ± 3.6
Fe-N-C	Fe-N_4	1.99 ± 0.02	3.8 ± 1.0	0.004 ± 0.003	-2.2 ± 3.3
Cu-N-C	Cu-N_4	1.92 ± 0.02	4.9 ± 1.1	0.007 ± 0.003	-4.8 ± 2.8
Co-N-C	Co-N_4	1.94 ± 0.04	4.4 ± 2.2	0.013 ± 0.007	-6.2 ± 6.0
	Co-Co	2.49 ± 0.01	2.3 ± 0.4	0.004 ± 0.002	-2.4 ± 2.0

and TEM images of Fe-N-C (**Figure S.7**) show atomically dispersed Fe sites. However, the fit for Co-N-C required the addition of a Co-Co path from a metallic Co CIF obtained from the materials

project database.[37] This suggests that there may be some Co nanoparticles present in addition to atomically dispersed Co-N_4 sites as has been observed previously in similar samples.[14]

3.2 Cyclohexane oxidation with TBHP – rates and kinetics across varied samples

3.2.1 *Kinetic Studies*

Before reporting initial rates or kinetic studies, the relevance of external diffusion limitations was accounted for by varying the stir rate in the reactor, and resulting in the conclusion that external mass transfer limitations were minimal at the 350 RPM stir speed used (See **Figure S.18**). The relevance of internal mass transfer limitations can be ignored, as the calculated Thiele modulus for $CuCl_{16}$PC@FAU was 0.00013 (much less than unity), suggesting internal mass transfer limitations are negligible (see **Section S.7** for more details).[68]

Previous reports have suggested involvement of O_2 (present in the headspace and/or dissolved in solutions from exposure to ambient air) in cyclohexane oxidation with TBHP.[6] To study any potential effect of oxidants present in the reactors (other than TBHP) on the rate of reaction, the possibility that atmospheric oxygen (present in the headspace of the reactors) may be playing a

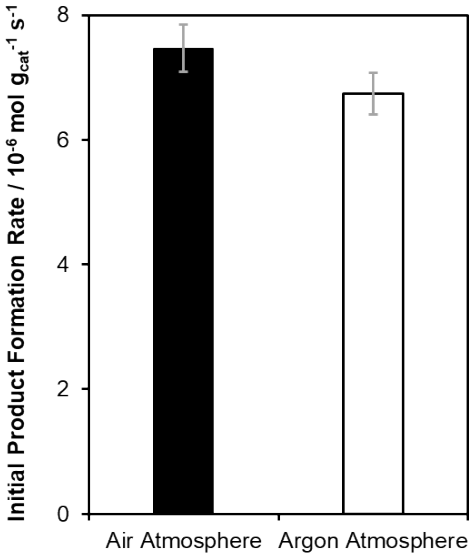

Figure 1. Initial combined product formation rate measured over Fe-N-C with air in the headspace (filled bar) and with argon in the headspace (empty bar). Reaction conditions: acetonitrile solvent, 1.05 M cyclohexane, 0.52 M TBHP, 312 K, 350 RPM, 1.8 ks, 0.020 g_{cat}.

role as an oxidizing agent for the oxidation of cyclohexane was considered. Filling the headspace with argon gas did not have a significant impact on the combined product formation rate, as shown in **Figure 1**.

The impact of the size and spatial orientation of the reactor on measured reactivity was also considered. First, a larger reactor with the same volume of reaction solution was used to determine if having a larger headspace and thus more available O_2 from air would increase the product formation rate, but this had no significant impact (See **Figure S.19**). Similarly, placing the reactor in the oil bath at an angle, thus increasing the surface area at the liquid-gas interface, also did not significantly impact the product formation rate (See **Figure S.19**).

A hot-filtration test was performed using Fe-N-C to confirm that metal centers were not leaching into the solution and participating in the reaction,. After a normal 0.15 ks batch reaction, the catalyst was separated from the reaction solution by filtration, and the filtered solution was

returned to the reactor to stir for an additional 1.8 ks at 312 K. The concentrations of cyclohexanol and cyclohexanone do not significantly change after removing the catalyst (**Figure S.20**), suggesting that metal centers are not leeching into the solution.

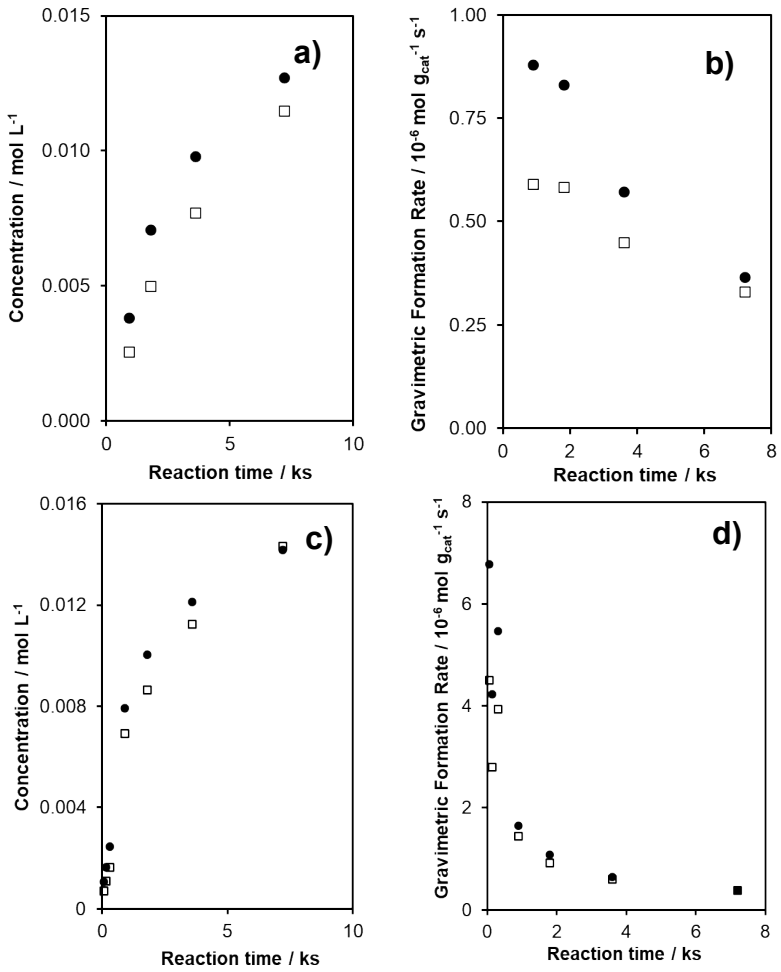

Figure 2. a) concentrations and b) gravimetric formation rates of cyclohexanol (filled circles) and cyclohexanone (open squares) during cyclohexane oxidation with $FeCl_{16}PC$/FAU. c) concentrations and d) gravimetric formation rates of cyclohexanol (filled circles) and cyclohexanone (open squares) during cyclohexane oxidation with Fe-N-C. Reaction conditions: acetonitrile solvent, 1.05 M cyclohexane, 0.52 M TBHP, 312 K, 350 RPM, 0.02 g_{cat}.

Reaction rates were assessed in liquid-phase batch reactors via the method of initial rates. To find a time when the initial concentration of cyclohexane was still available, product concentrations and gravimetric formation rates were monitored after different reaction batch times at 312 K over $FeCl_{16}PC$/FAU (**Figure 2 a,b**), Fe-N-C (**Figure 2 c,d**) and other MPC/FAU samples (**Figure S.23**). The initial rate measurements (**Figure 2 b,d**) indicate that initial rates are constant up to 1.8 ks for MPC samples, but that initial reaction rates decrease significantly after only 0.15 ks for M-N-Cs. As a result, as Fe-containing samples were the most reactive in this study (*vide infra*), initial rates were calculated for reaction times that were no longer than 1.8 ks for MPC samples, and at most 0.15 ks for M-N-C samples.

The initial concentrations of cyclohexane and TBHP were varied to determine the apparent reaction orders (**Figure 3**). Across the range of concentrations tested, cyclohexane oxidation over $FeCl_{16}PC$@FAU (**Figure 3**, filled circles) was approximately first order with respect to cyclohexane and ~0.4 order with respect to TBHP. These results are similar to those measured

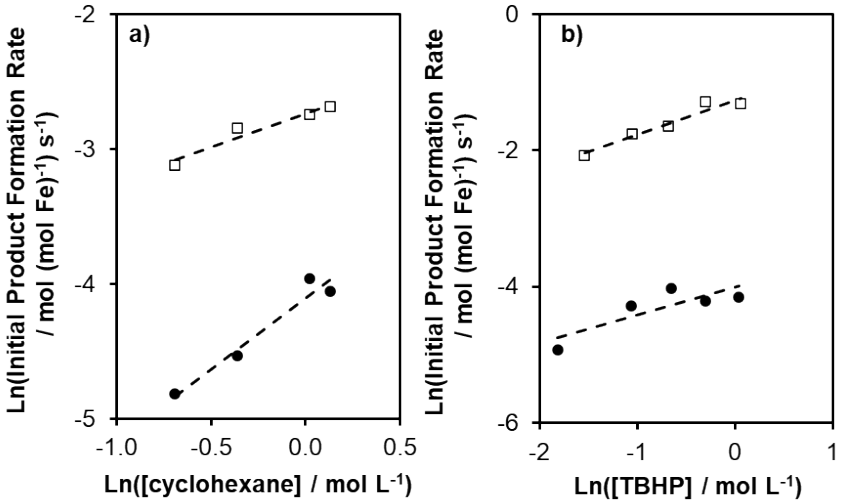

Figure 3. Natural log of combined gravimetric product formation rate over $FeCl_{16}PC$@FAU (filled circles) and Fe-N-C (open squares) at different starting concentrations of a) cyclohexane and b) TBHP used to estimate apparent reaction orders. Reaction conditions: acetonitrile solvent, 0.5-1.15 M cyclohexane, 0.17-1.05 M TBHP, 312 K, 350 RPM, 0.15 ks for Fe-N-C or 1.8 ks for $FeCl_{16}PC$@FAU.

over Fe-N-C (**Figure 3**, open squares) with respect to TBHP, however the reaction appears to also be ~0.5 order with respect to cyclohexane over Fe-N-C. Apparent reaction orders with respect to both reactants have not been directly measured previously for this reaction, to our knowledge, but

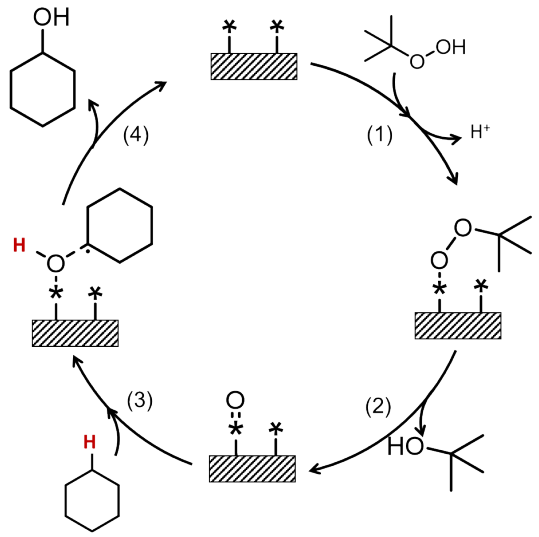

Scheme 1. Mechanism of cyclohexane oxidation with TBHP over FePC proposed by Parton and coworkers.[26]

were assumed to be first order by Parton et al. (298 K, 0.67 M cyclohexane, 2.7 M TBHP, acetone solvent),[8] found to be pseudo-first order with respect to cyclohexane by Mahdavi et al. (300 K, 0.22 M cyclohexane, 3.3 M TBHP, acetonitrile solvent),[69] and second order with respect to cyclohexane by Rekkab-Hammoumraoui et al. (298 K, 0.92 M cyclohexane, 0.92 M TBHP, acetic acid solvent).[70] Since rates measured here over $FeCl_{16}PC$@FAU appeared to be first order with

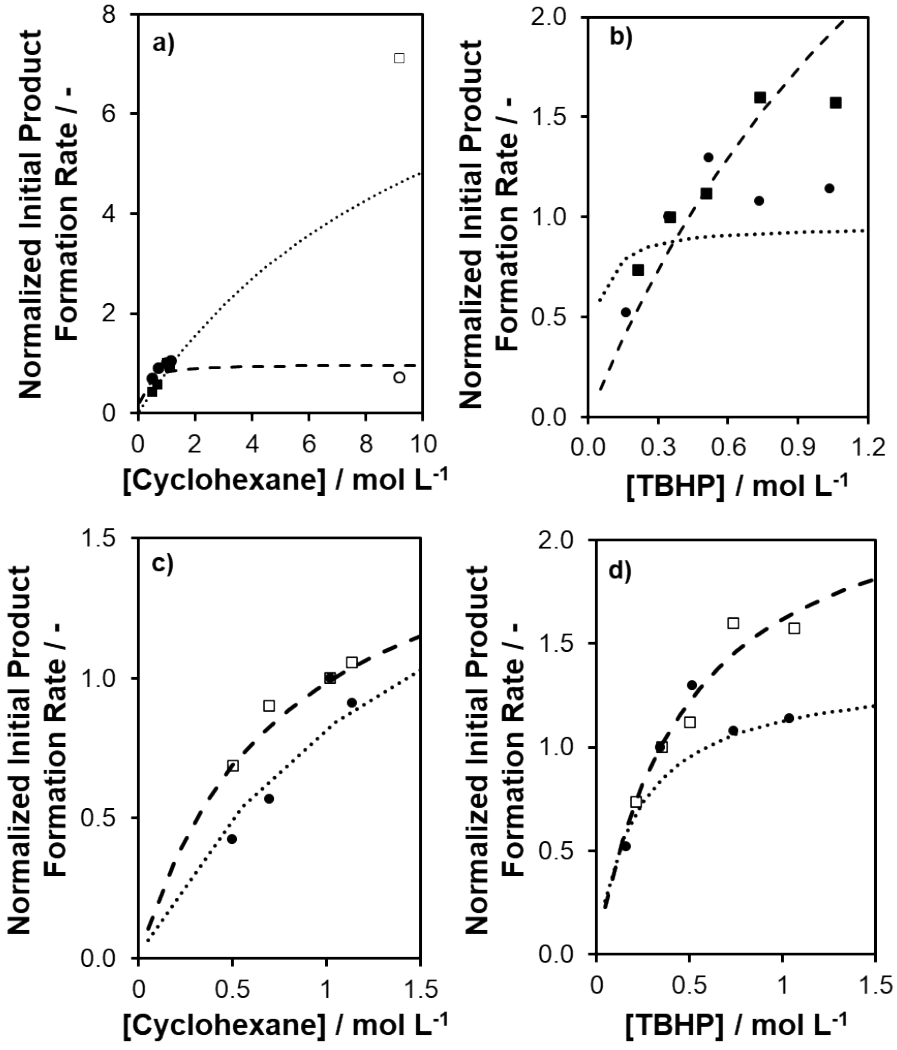

Figure 4. Measured combined gravimetric product formation rate normalized by rate at standard conditions over $FeCl_{16}PC$@FAU (circles) and Fe-N-C (squares) at different starting concentrations of a) cyclohexane and b) TBHP along with rates predicted by eq. 7 after regressing data measured over $FeCl_{16}PC$@FAU (dotted) and Fe-N-C (dashed). Panels c) and d) are the same model with the exclusion of data measured in pure cyclohexane. Reaction conditions: acetonitrile solvent, 0.5-1.15 M cyclohexane, 0.17-1.05 M TBHP, 312 K, 350 RPM, 0.15 ks for Fe-N-C or 1.8 ks for $FeCl_{16}PC$@FAU.

respect to cyclohexane (as assumed by Parton and coworkers[26]), this mechanism was considered first, as outlined in **Scheme 1.** This mechanism notably does not include the formation of cyclohexyl hydroperoxide (CHHP), which has been observed as a product in cyclohexanol and cyclohexanone formation using TBHP.[38] Another study done by Parton and coworkers on the oxidation of cyclohexane with TBHP over FePC@FAU reported that no CHHP was observed in

their product solutions,[8] though no in-depth mechanistic study was reported. As such, we did not consider any mechanisms including CHHP in this study. To derive a rate expression from **Scheme 1**, the pseudo-steady-state hypothesis (PSSH) was applied to the reactive intermediates in steps 1 and 2, and the H-abstraction (step 3) was assumed to be the rate determining step as proposed by Parton et al.,[26] resulting in eq. 15 (See **Section S.10** for derivation).

$$\frac{r_{net}}{[L]} = \frac{k_2 k_1 [\text{TBHP}]}{1+\frac{k_2 k_1 [\text{TBHP}]}{k_3 [\text{cyclohexane}]}} \quad (15)$$

Since k_1 and k_2 are always coupled in eq. 15, they were modeled as one combined term, k_1k_2. This model captures trends relatively well (**Figure 4**) for data measured in acetonitrile solvent for $FeCl_{16}PC$@FAU with respect to cyclohexane and Fe-N-C with respect to both reactants, however, the model fails to describe activity measured in pure cyclohexane (open symbols in **Figure 4a**) for both samples. Panels c and d in **Figure 4** show how the fit of this model improves when data measured in pure cyclohexane is excluded. The model now captures trends for both Fe-N-C and $FeCl_{16}PC$@FAU with respect to both cyclohexane and TBHP. Parity and residual plots for this model both with and without data measured in pure cyclohexane can be found in **Section S.11**.

To find a model that would capture data measured in pure cyclohexane, a Langmuir-Hinshelwood (LH) mechanism was considered, which is similar to the model proposed by Becerra et al. for the oxidation of α-pinene with TBHP over $FeCl_{16}PC/SiO_2$ and reported in **Scheme 2.**[71] To derive a rate expression from this mechanism, the reactant adsorption steps (steps 1 and 2) were assumed to be quasi-equilibrated, and step 3, the reaction of the two adsorbed species, was assumed to be the rate determining step as proposed by Becerra and coworkers,[71] resulting in eq. 16 (See **Section S.10** for derivation).

$$\frac{r_{net}}{[L]} = \frac{k_3 K_1 K_2 [\text{cyclohexane}][\text{TBHP}]}{(1+K_2[TBHP]+K_1[cyclohexane])^2} \quad (16)$$

The LH model, unlike the model proposed by Parton and coworkers (with regression results shown in **Figure 4**),[26] appears to describe rates measured in acetonitrile solvent and pure cyclohexane over $FeCl_{16}PC$@FAU and Fe-N-C (**Figure 5**). Normalized residuals are smaller, and data follows

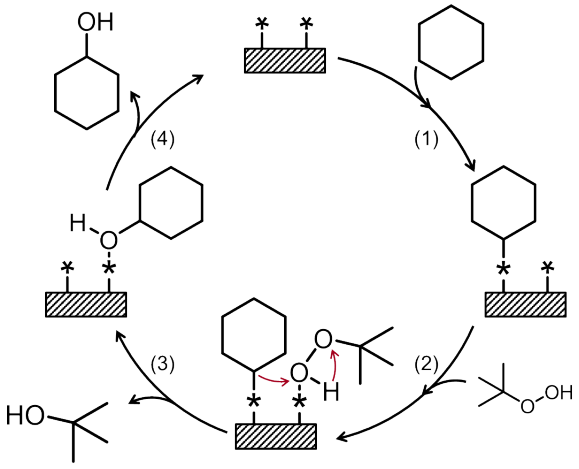

Scheme 2. Langmuir-Hinshelwood mechanism for cyclohexane oxidation with TBHP over FePC modified from Becerra and coworkers.[63]

the parity line more closely for the LH model compared to the mechanism from **Scheme 1** and eq. 15 (see **Section S.11** for parity and residual plots). The main reason for the improved fit of the LH model compared to the Parton model is due to the inclusion of data measured in pure cyclohexane. Additional experiments with higher concentrations of cyclohexane in acetonitrile would be necessary to confirm that the LH model more closely follows observed trends. Further investigation of these potential reaction pathways was performed using computational catalysis approaches.

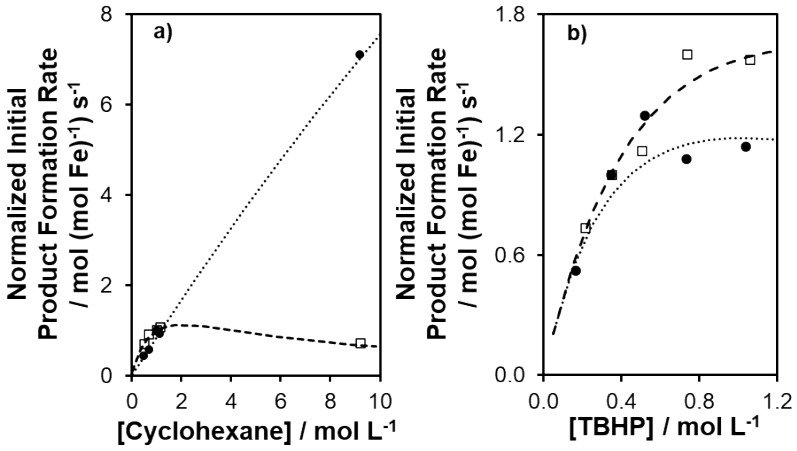

Figure 5. Measured combined gravimetric product formation rate normalized by rate at standard conditions over $FeCl_{16}PC$@FAU (circles) and Fe-N-C (squares) at different starting concentrations of a) cyclohexane and b) TBHP along with rates predicted by eq. 8 after regressing data measured over $FeCl_{16}PC$@FAU (dotted) and Fe-N-C (dashed). Reaction conditions: acetonitrile solvent, 0.5-1.15 M cyclohexane, 0.17-1.05 M TBHP, 312 K, 350 RPM, 0.15 ks for Fe-N-C or 1.8 ks for $FeCl_{16}PC$@FAU.

Apparent activation energies were calculated using the Arrhenius equation for initial rates measured between 312-342 K. Over Fe-N-C, $FeCl_{16}PC$/FAU, and $FeCl_{16}PC$@FAU (**Figure 6)**, the apparent activation energies were 22.1 ± 2.6 kJ mol^{-1}, 24.4 ± 6.0 kJ mol^{-1}, and 54.2 ± 8.7 kJ mol^{-1}, respectively, consistent with previous reports of oxidation chemistries with TBHP over Co-N-C[72] and $FeCl_{16}PC/SiO_2$,[71] as well as cyclohexane oxidation with TBHP over Co promoted vanadium phosphorous oxide (VPO)[69] and ruthenium nanoparticles supported on alumina.[70]

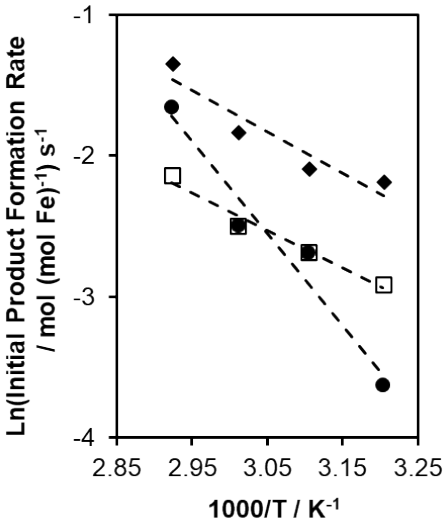

Figure 6. Arrhenius plot used to determine apparent activation energies over $FeCl_{16}PC$/FAU (filled diamonds), Fe-N-C (open squares), and $FeCl_{16}PC$@FAU (filled circles). Reaction conditions: acetonitrile solvent, 1.05 M cyclohexane, 0.52 M TBHP, 312-342 K, 350 RPM, 0.15 ks for Fe-N-C or 1.8 ks for $FeCl_{16}PC$@FAU and $FeCl_{16}PC$/FAU, 0.010 g_{cat}.

3.2.2 Comparison of initial rates across MPCs and MNCs

Gravimetric rates of KA oil production are shown in **Figure 7a**. All data shown in **Figure 7a** was collected after 1.8 ks of reaction for comparison purposes. Samples with Fe active sites ($FeCl_{16}PC$/FAU, $FeCl_{16}PC$@FAU, and Fe-N-C) had higher initial rates than all other transition metals for all three types of samples tested (MPC@FAU, MPC/FAU, MNC). Na/FAU and metal-free N-C were also tested as control experiments and showed minimal activity (see **Figure S.21**); the rates measured over these control samples were subtracted from the rates shown in **Figure 7**. $MnCl_{16}PC$/FAU also had a higher product formation rate than the $MnCl_{16}PC$ complex with no support, suggesting that the presence of a support is beneficial (See **Figure S.22**), which has been reported previously.[73, 74] The trend in rates across the first-row transition metals is different over MPC vs M-N-C samples, as $MnCl_{16}PC$ samples had the second highest initial rates of the MPC samples tested, but Mn-N-C had the lowest initial rate of the M-N-C samples tested. $CuCl_{16}PC$/FAU and NiPC/FAU were also tested but no products were observed. Normalizing the rates per mol of metal results in similar trends (**Figure 7b**). Per-metal-atom turnover numbers (TON) for these data are reported in **Table S.2**.

Normalizing per mol of metal atoms results in MPC/FAU and MPC@FAU site-time-yields (STYs) that are similar, suggesting limited benefits on reactivity of confining and/or isolating MPCs within FAU crystallites relative to dispersing them on the exterior of FAU. The STYs reported in **Figure 7** likely reflect a lower bound on the turnover frequency for all samples, but particularly for M-N-C samples for which a broad distribution of M species is likely present. Bates and co-workers[12] reported various synthetic approaches to produce Fe-N-Cs, including the pyrolysis of ZIF-8 employed here. In that case, it was determined that ~50% of the Fe sites were $Fe\text{-}N_4$-C sites active in hydroquinone oxidation.[12] As such, it is likely that the per-$Fe\text{-}N_4$ STYs for M-N-Cs are higher than those shown in **Figure 7**.

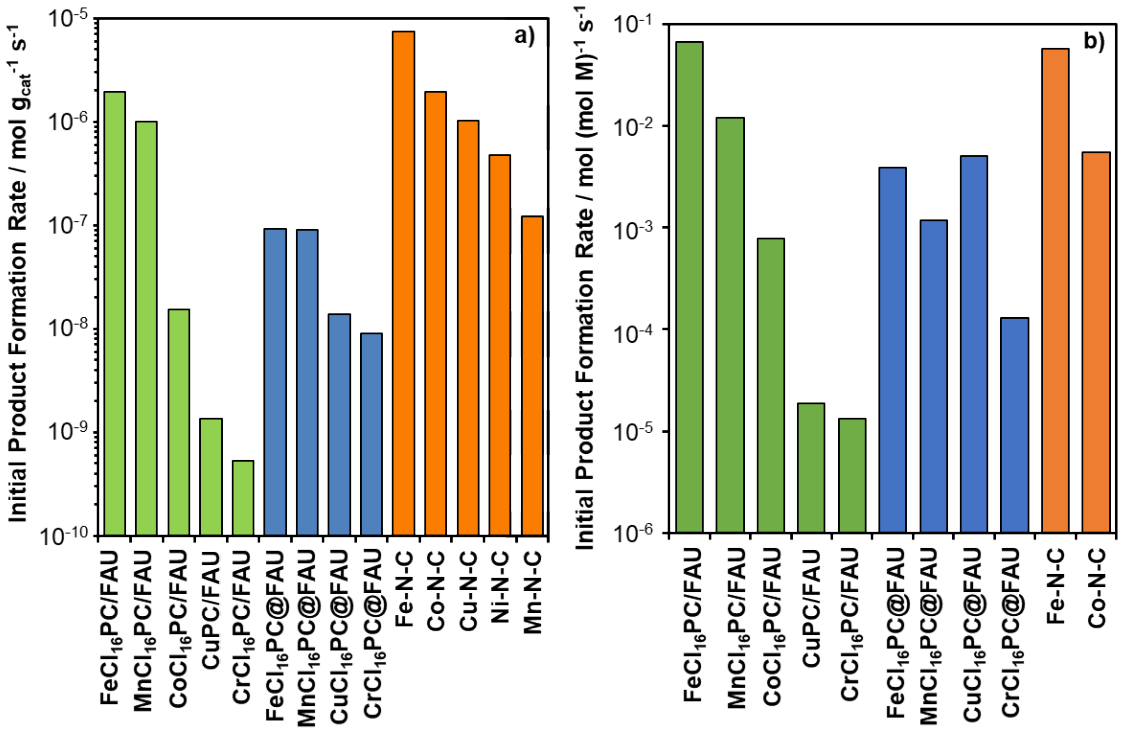

Figure 7. Initial (a) gravimetric and (b) molar combined product formation rate measured over all samples tested. Reaction conditions: acetonitrile solvent, 1.05 M cyclohexane, 0.52 M TBHP, 312 K, 350 RPM, 0.020 g_{cat}, 1.8 ks.

The phthalocyanine complex has sixteen peripheral hydrogens that can be substituted to tune the properties of the complex.[27, 75] Substituting these hydrogens for a more electron withdrawing group, such as a halogen, increased the initial gravimetric KA oil formation rate, as shown in **Figure 8**. This result differs from our previous work studying gas phase CO oxidation, where reactant binding energies do not vary significantly due to the identity of the peripheral ligands.[28] Reactivity increasing as the peripheral substituent becomes more electron withdrawing is consistent with observations made by Seelan et al.[75] during styrene epoxidation with TBHP over CuPC samples in the liquid phase.

Lastly, the reusability of MPC and M-N-C catalysts was investigated. Catalysts were separated from the product solutions after reaction by centrifugation and dried overnight under vacuum at 363 K. Significant deactivation was observed for both $FeCl_{16}PC/FAU$ and $FeCl_{16}PC@FAU$, while Fe-N-C was stable with repeated use, as shown in **Figure (S.27)**. It is possible that the deactivation observed over MPC samples is due to degradation of the MPC complex by TBHP radicals.[76-78] As is evident from **Figure (S.27),** confining and/or isolating MPCs within FAU zeolites has limited benefit on the stability of the MPCs against oxidative decomposition in the presence of TBHP and/or hydroxyl radicals. As such, it is possible that intrinsic initial rates measured over MPC samples are slightly higher than those reported in **Figure 7.**

3.2.6 Product selectivity

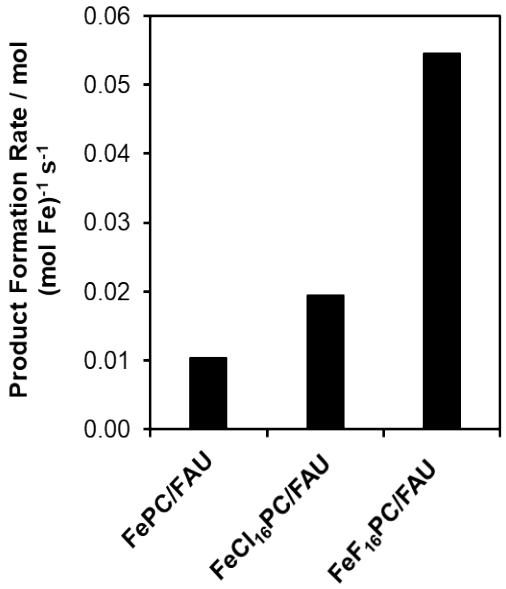

Figure 8. Initial combined product formation rate measured over FePC/FAU samples with different peripheral substituents. Reaction conditions: acetonitrile solvent, 1.4 M cyclohexane, 0.52 M TBHP, 312 K, 350 RPM, 0.020 g_{cat}.

Cyclohexane oxidation with TBHP forms both cyclohexanol and cyclohexanone. Both products are present after short reaction times (**Figure 2**), before cyclohexanone selectivities increase with increasing reaction time, and similar trends are observed with selectivity and increasing conversion of both reactants. (**Figure 9**). This suggests that a portion of the cyclohexanone produced could form in a parallel pathway, such as might be expected via Gif chmiestry,[79] rather than solely through successive oxidation of cyclohexane to cyclohexanol, and of cyclohexanol to cyclohexanone. To probe the mechanistic origins of these products, and the potential for a parallel pathway in addition to a series pathway, we turned to density functional theory calculations as discussed in the next section.

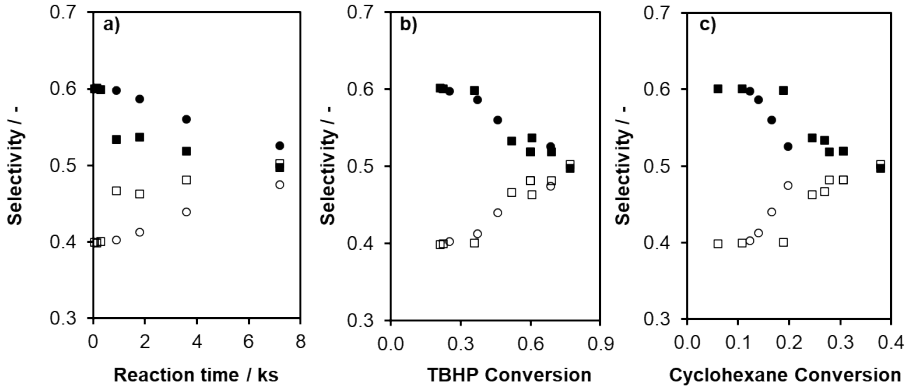

Figure 9. Selectivity to cyclohexanol (filled markers) and cyclohexanone (open markers) plotted against batch a) reaction time, b) TBHP conversion, and c) cyclohexane conversion over $FeCl_{16}PC$@FAU (circles) and Fe-N-C (squares). Reaction conditions: acetonitrile solvent, 1.05 M cyclohexane, 0.52 M TBHP, 312 K, 350 RPM, 0.020 g_{cat} for $FeCl_{16}PC$@FAU, 0.010 g_{cat} for Fe-N-C.

3.2.7 Computational Results

To support experimental results, the experimental results were considered as inputs to computational reaction mechanism discovery. **Scheme 3** shows the overall reaction considered for cyclohexane oxidation to cyclohexanol and cyclohexanone via a radical-mediated Eley-Rideal mechanism, as proposed in previous studies.[80, 81] Since our previous work showed that modeling the MPC as a single unit in vacuum is a reasonable assumption,[1] calculations were carried out using a single $FeH_{16}PC$ in vacuum as the catalyst.[28]

Batch reactions of various durations over $FeCl_{16}PC$/FAU showed that the catalyst is initially more selective towards cyclohexanol (60% selectivity) over cyclohexanone (40% selectivity), however as the reaction proceeds selectivity approaches 50% for each product (**Figure**

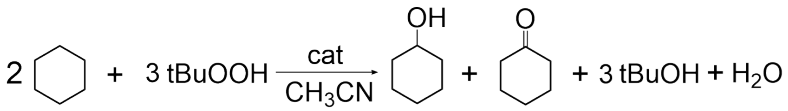

Scheme 3. Overall reaction for cyclohexane oxidation.

9). This suggests that there may be a combination of parallel and serial reaction pathways, of which the latter involves oxidation of cyclohexanol to cyclohexanone. Consequently, the interconnected reaction mechanisms and elementary steps shown in **Scheme 4** were studied. Here, there are two parallel pathways leading to cyclohexanol and cyclohexanone. For the cyclohexanol branch, the reaction cycle begins by binding TBHP to the metal site (step 1) which is then followed by the dissociation of TBHP to form a radical (tBuO) and leaves behind a metal-bound OH (step 2). The tBuO radical then abstracts a hydrogen atom from cyclohexane to form *tert*-butanol (tBuOH) and a cyclohexyl radical ($Cy_H^{\cdot}$ in **Scheme 4,** step 5). Next, the cyclohexyl radical combines with the metal-bound OH to form a metal-bound cyclohexanol (step 7) which can subsequently be released into the liquid phase (step 8), thus closing the catalytic cycle. For the cyclohexanone branch, the reaction proceeds as described above but branches off at the Fe-OH intermediate (after step 2) whereby another TBHP reacts with the bound OH to form water and a metal-bound tBuOO (step 3). The bound tBuOO then decomposes into a tBuO radical and leaves behind a metal-oxo complex (step 4). The produced tBuO radical further reacts with the cyclohexyl radical and abstracts a second hydrogen atom to form tBuOH and a cyclohexyl radical with a lone pair of electrons (Cy: in **Scheme 4,** step 6). This cyclohexyl radical then combines with the metal-oxo complex to form a metal bound cyclohexanone (step 9) which can then be released into the liquid phase (step 10). Additionally, the produced cyclohexanol can also react with the metal-oxo complex to form a metal bound diol that decomposes to form water and cyclohexanone (steps 11-13).

To validate the proposed mechanism, MKM was carried out in COPASI to obtain product selectivities, the most abundant metal intermediate, and time-on-stream data that are directly comparable to experimental results. As shown in **Figure 10**, at the start of the reaction, cyclohexanol is the predominant product and after 1.8 ks, the cyclohexanol to cyclohexanone ratio is ~1.5, which is comparable to what was obtained from experimental measurements. We note that the selectivity initially starts at 100% towards cyclohexanol in **Figure 10**, but this result is difficult to compare to experiments since the time scale is too small for experimental measurements. Nonetheless, the computational results also indicate after the initial transient period that selectivity towards cyclohexanol is 60%, in agreement with experimental results (**Figure 9**).

As the reaction proceeds, cyclohexanol is gradually consumed and after 7.2 ks the ratio of cyclohexanol to cyclohexanone decreases to unity (i.e., 50% selectivity towards both oxidation products). These results indicate that at the initiation of the reaction, cyclohexanol production is the predominant mechanism occurring, but as cyclohexanol accumulates in the system, the cyclohexanone mechanism becomes more prominent as cyclohexanol is consumed to produce cyclohexanone. Thus, the computational results accurately reproduce the experimentally observed selectivity and reactivity trends shown in **Figure 9** without any parameter fitting, suggesting the proposed mechanism is reasonable. Parameter estimation was not performed, due to experimental limitations in obtaining a sufficient number of time-on-stream data points that such computations could be used without overfitting. In addition, rates collected in pure cyclohexane solvent (**Figure 5**) could not be modelled computationally due to the limitations of implicit solvation. For these reasons, the computational results were not fit to the experimental data. The MKM predicts the

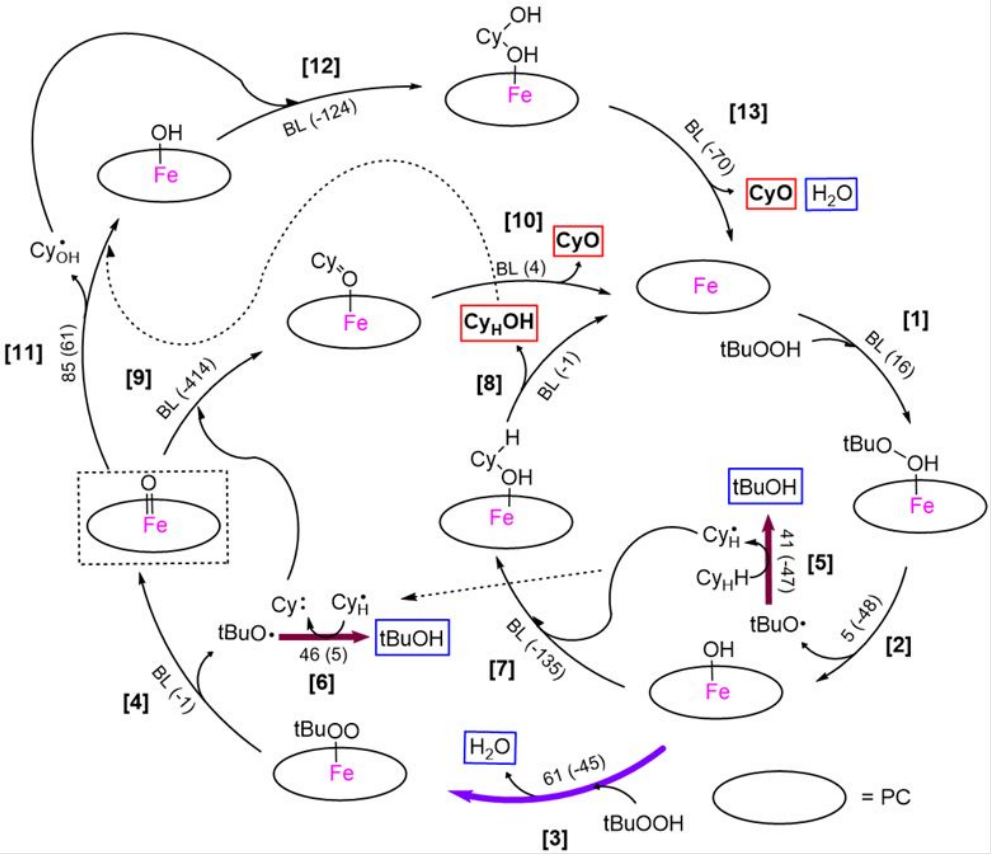

Scheme 4. Reaction pathways studied using density functional theory calculations for cyclohexane oxidation on $FeH_{16}PC$. Values within parenthesis represent the Gibbs free energy of reaction in kJ mol^{-1}, values outside the parenthesis represent the activation Gibbs free energy in kJ mol^{-1}, and 'BL' refers to an activation energy barrierless elementary step. Bold numbers in square brackets represent the numbering of the reaction steps. Cyclohexane and TBHP are represented as Cy_HH and tBuOOH, respectively. The *tert*-butoxy radical is represented by $tBuO\cdot$, and the cyclohexyl radicals are denoted as $\dot{Cy}_H$ and Cy:, respectively, while the cyclohexanol radical is represented as $\dot{Cy}_{OH}$. Species in red boxes are the main products of the reaction (CyO = cyclohexanone, Cy_HOH = cyclohexanol) while species in blue boxes are side products of the reaction (H_2O = water, and tBuOH = *tert*-butanol). The species in the dashed black box was noted as the most abundant metal intermediate in the microkinetic modeling. Solid black lines represent the main reaction pathways, dashed lines show that the indicated specie participates in a different branch of the reaction mechanism, while the purple and brown bolded solid lines represent the elementary steps that control the cyclohexanol and cyclohexanone production rates, respectively, according to sensitivity analysis.

Fe=O intermediate to be the most abundant under reaction conditions, which could be probed through spectroscopic measurements in the future.

To give further insights into the rate determining steps for the reaction, a sensitivity analysis of the cyclohexanone and cyclohexanol production rates to rate constants of the elementary steps considered in **Scheme 4** was performed. The cyclohexanone formation

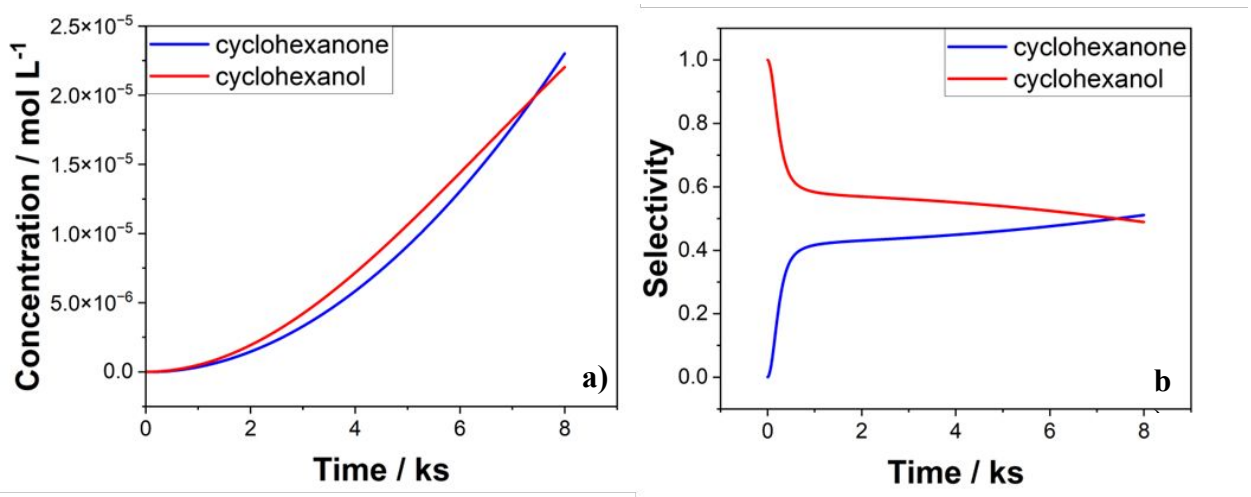

Figure 10. a) Concentration of cyclohexanol and cyclohexanone as a function of time and b) selectivity of cyclohexanol and cyclohexanone as a function of reaction time from microkinetic modeling studies.

rate was only sensitive to two steps, the *tert*-butyl radical assisted hydrogen abstractions from cyclohexane and cyclohexyl radical. Increasing the rate of hydrogen abstraction from the cyclohexyl radical increases the rate of cyclohexanone production, resulting in a sensitivity coefficient of unity (see **Table S.4)**. Since the Cy: radical combines with the Fe=O intermediate to form metal bound cyclohexanone, producing more Cy: radicals increases the cyclohexanone formation rate. On the other hand, increasing the rate of the first hydrogen abstraction from cyclohexane reduces the cyclohexanone formation rate, resulting in a sensitivity coefficient of -1. The free energy barrier for the hydrogen abstraction from cyclohexane (41 kJ mol^{-1}) is lower than that for the second hydrogen abstraction (46 kJ mol^{-1}), thus further reduction in the free energy barrier (i.e. increasing the rate) results in an even greater proportion of the cyclohexyl radicals that rebound to the Fe-OH intermediate. Consequently, less Cy: radicals will be formed that lead to the formation of cyclohexanone.

Meanwhile for cyclohexanol, its formation rate is only sensitive to the formation of the Fe-OOR species and the hydrogen abstraction from cyclohexanol. Here, increasing the formation rate of the Fe-OOR intermediate decreases the cyclohexanol formation rate with a sensitivity coefficient of -1, while increasing the hydrogen abstraction rate from cyclohexanol decreases the cyclohexanol rate with a sensitivity coefficient of -0.7. The sensitivity coefficient of -1 for the cyclohexanol formation rate implies that Fe-OH is the selectivity-determining intermediate, since this intermediate is the intersection point of the parallel pathways that produce either cyclohexanol or cyclohexanone. Consequently, increasing the formation rate of the Fe-OOR intermediate increases the flux through the cyclohexanone pathway, and less cyclohexanol is produced. Likewise, increasing the rate of hydrogen abstraction from cyclohexanol reduces the formation rate of cyclohexanol (sensitivity coefficient of -0.7) since the rate of cyclohexanol consumption

increases. In addition to the sensitivity analysis, we also carried a degree of selectivity control (X_{SC}) analysis. Table S.3 shows that only three steps control the selectivity (i.e. cyclohexanol rate/cyclohexanone rate). Here, we see that the Fe-tBuOO formation step, and the hydrogen abstraction from the cyclohexyl radical reduces selectivity towards cyclohexanone production with a X_{SC} of -1 and -0.5, respectively. On the other hand, the hydrogen abstraction from cyclohexane step promotes selectivity towards cyclohexanol with an X_{SC} of 1.0. The X_{SC} analysis is also consistent with the sensitivity analysis which showed that the hydrogen abstraction steps from the cyclohexane/cyclohexyl radical in addition to the production of the Fe-tBuOO intermediate control the selectivity of the reaction. These computational results suggest that the oxidation of cyclohexane to cyclohexanol and cyclohexanone may proceed via a radical-rebound/radical-mediated Eley-Rideal mechanism, similar to the mechanism proposed by Parton and coworkers.[26] The results reported here also show that the Fe-OH intermediate, the relative abundance of the cyclohexyl radicals ($\dot{Cy}_H$ and Cy:), and the Fe=O mediated hydrogen abstraction from cyclohexanol collectively determine the relative formation rates of cyclohexanol and cyclohexanone during the oxidation of cyclohexane with TBHP.

4. Conclusions

Catalysts containing M-N_4 primary binding sites are emerging materials for a range of chemical reactions. Here, the oxidation of cyclohexane with TBHP was used as a probe reaction to compare the reactivity of a series of metal phthalocyanine and metal-nitrogen-doped carbon catalysts. MPCs were encapsulated within FAU zeolites via hydrothermal synthesis and dispersed on the exterior of FAU. M-N-C samples were prepared by pyrolysis of ZIF-8 precursors, or by pyrolysis of Co and 1,10-phenanthroline with amorphous carbon. Materials were characterized by XRD, N_2 adsorption, DRUV-Vis and XAS. These methods determined that the MPC structure remains intact in all MPC catalysts. Along with TEM, these methods determined that M-N-C samples had predominantly isolated metal atoms.

After confirming a lack of internal or external diffusion limitations on the measured rates and determining that atmospheric O_2 did not impact measured rates, initial rates of cyclohexane oxidation were measured for the suite of samples. Initial rates were higher over M-N-C samples compared to MPC@FAU and MPC/FAU catalysts for a given metal identity. Samples with Fe binding sites had the highest initial rates for both MPC and M-N-C catalysts. Reaction over $FeCl_{16}$PC@FAU appears to be first order with respect to cyclohexane, while all other apparent reaction orders with respect to cyclohexane and TBHP were less than one. Attempts to regress data to previously reported mechanisms for cyclohexane oxidation with TBHP over MPC catalysts captured the observed trends well for rates measured in dilute cyclohexane in acetonitrile, but were unable to capture rates measured in pure cyclohexane. The full data set was described well by a rate expression determined by considering a Langmuir-Hinshelwood reaction mechanism, but additional experiments with higher concentrations of cyclohexane in acetonitrile would be necessary to validate this pathway. Apparent activation energies were consistent with previous reports of cyclohexane oxidation with TBHP, as well as oxidation reactions with TBHP over M-N-C and MPC catalysts. M-N-C catalysts were stable with repeated use, while MPC catalysts had reduced reactivity upon reuse.

Both cyclohexanol and cyclohexanone formed at short reaction times, before cyclohexanone selectivity increased at longer reaction times. These results indicate the presence of a parallel pathway for formation of cyclohexanol and cyclohexanone from cyclohexane, in addition to a series pathway to cyclohexanone via cyclohexanol. Microkinetic modeling studies also showed

that cyclohexanol and cyclohexanone are produced in parallel with cyclohexanol initially being the major product. However, at long reaction times cyclohexanol was also converted into cyclohexanone thus increasing the selectivity towards cyclohexanone. Fe-OH was identified as a key selectivity determining intermediate that lies at the branching point for formation of either cyclohexanol or cyclohexanone.

This study demonstrates that isolated MPCs dispersed on solid supports have similar reactivity to M-N-C catalysts, and that all of these materials catalyze the oxidation of cyclohexane with TBHP. Apparent kinetics for this well-studied probe reaction are reported, and the pathway from cyclohexane to cyclohexanol and cyclohexanone is probed both experimentally and computationally. Experimental results suggest this reaction proceeds via either a Langmuir-Hinshelwood or an Eley-Rideal type mechanism over both MPC and M-N-C catalysts, meanwhile, DFT studies suggested a radical-rebound/radical-mediated Eley-Rideal mechanism over MPC that also reproduces selectivity trends without performing any parameter estimation/fitting. These results provide guidance regarding the most reactive metal binding sites and stability considerations for future researchers investigating liquid-phase oxidation chemistries over catalysts with $M\text{-}N_4$ active sites.

Declaration of Competing Interest

The authors declare no competing financial interests.

Acknowledgements

A.S. and T.S. would like to thank the University of Alabama and the Office of Information Technology for providing high-performance computing resources and support that has contributed to these research results. This work was also made possible in part by a grant of high-performance computing resources and technical support from the Alabama Supercomputer Authority. This research also used resources of the National Energy Research Scientific Computing Center (NERSC), a U.S. Department of Energy Office of Science User Facility located at Lawrence Berkeley National Laboratory, operated under Contract No. DE-AC02-05CH11231. A.S. would also like to acknowledge the financial support of the University of Alabama Graduate School as a Graduate Council Fellow. The authors acknowledge financial support from the National Science Foundation through award numbers 2050507 and 2327267, and from the Alabama Graduate Research Scholars Program (GRSP) funded through the Alabama Commission for Higher Education and administered by the Alabama EPSCoR. We acknowledge Eli Stavitski and Akhil Tayal (ISS team at NSLS-II) for support with XAS data collection and analysis.

Appendix A. Supplementary material

Supplementary data to this article can be found online free of charge, and includes: XRD patterns, N_2 adsorption isotherms, DRUV spectra, XAS data, assessments of hydrodynamic effects, Batch time data, rate expression derivations, regression analysis.

References

1. E. C. Botelho, N. Scherbakoff, M. C. Rezende, A. M. Kawamoto and J. Sciamareli, *Macromolecules*, 2001, **34**, 3367-3375.
2. M. Pelckmans, T. Renders, S. Van de Vyver and B. F. Sels, *Green Chemistry*, 2017, **19**, 5303-5331.

3. J. B. J. H. van Duuren, B. Brehmer, A. E. Mars, G. Eggink, V. A. P. M. dos Santos and J. P. M. Sanders, *Biotechnology and Bioengineering*, 2011, **108**, 1298-1306.
4. M. A. Andrade and L. M. D. R. S. Martins, *Catalysts*, 2020, **10**.
5. R. Mewada, *International Journal of Engineering Development and Research*, 2014, **2**, 3911-3914.
6. R. Raja and P. Ratnasamy, *Catalysis Letters*, 1997, **48**, 1-10.
7. M. das Dores Assis, O. A. Serra, Y. Iamamoto and O. R. Nascimento, *Inorganica Chimica Acta*, 1991, **187**, 107-114.
8. R. F. Parton, G. J. Peere, P. E. Neys, P. A. Jacobs, R. Claessens and G. V. Baron, *Journal of Molecular Catalysis A: Chemical*, 1996, **113**, 445-454.
9. B. Meunier, *Metalloporphyrins catalyzed oxidations*, 1994, 1-47.
10. T. Onodera, S. Suzuki, T. Mizukami and H. Kanzaki, *Journal of Power Sources*, 2011, **196**, 7994-7999.
11. M. Lefèvre, E. Proietti, F. Jaouen and J.-P. Dodelet, *Science*, 2009, **324**, 71-74.
12. J. S. Bates, F. Khamespanah, D. A. Cullen, A. A. Al-Omari, M. N. Hopkins, J. J. Martinez, T. W. Root and S. S. Stahl, *Journal of the American Chemical Society*, 2022, **144**, 18797-18802.
13. J. Xie, K. Yin, A. Serov, K. Artyushkova, H. N. Pham, X. Sang, R. R. Unocic, P. Atanassov, A. K. Datye and R. J. Davis, *ChemSusChem*, 2017, **10**, 359-362.
14. J. Xie, J. D. Kammert, N. Kaylor, J. W. Zheng, E. Choi, H. N. Pham, X. Sang, E. Stavitski, K. Attenkofer, R. R. Unocic, A. K. Datye and R. J. Davis, *ACS Catalysis*, 2018, **8**, 3875-3884.
15. C. A. Whitcomb, A. Shrestha, C. Paolucci and R. J. Davis, *Catalysis Science & Technology*, 2024, **14**, 2479-2488.
16. L. Chen, Y. Sun, J. Chi, W. Xiong, P. Liu and F. Hao, *Frontiers of Chemical Science and Engineering*, 2024, **18**, 33.
17. F. Hao, Y. Sun, Y. Wang, Y. Lv, P. Liu, W. Xiong and H. Luo, *Korean Journal of Chemical Engineering*, 2021, **38**, 1608-1616.
18. P. Chen, T. Zhou, L. Xing, K. Xu, Y. Tong, H. Xie, L. Zhang, W. Yan, W. Chu, C. Wu and Y. Xie, *Angewandte Chemie International Edition*, 2017, **56**, 610-614.
19. K. Gong, F. Du, Z. Xia, M. Durstock and L. Dai, *Science*, 2009, **323**, 760-764.
20. E. P. Iaia, A. Soyemi, T. Szilvási and J. W. Harris, *Dalton Transactions*, 2023, **52**, 16103-16112.
21. E. Armengol, A. Corma, V. Fornés, H. García and J. Primo, *Applied Catalysis A: General*, 1999, **181**, 305-312.
22. K. J. Balkus Jr, M. Eissa and R. Levado, *Journal of the American Chemical Society*, 1995, **117**, 10753-10754.
23. K. J. Balkus, M. Eissa and R. Lavado, *Studies in Surface Science and Catalysis*, 1995, **94**, 713-719.
24. K. J. Balkus, A. K. Khanmamedova, K. M. Dixon and F. Bedioui, *Applied Catalysis A: General*, 1996, **143**, 159-173.
25. F. Thibault-Starzyk, R. F. Parton and P. A. Jacobs, in *Studies in Surface Science and Catalysis*, Elsevier, 1994, vol. 84, pp. 1419-1424.
26. R. F. Parton, P. E. Neys, P. A. Jacobs, R. C. Sosa and P. G. Rouxhet, *Journal of Catalysis*, 1996, **164**, 341-346.
27. R. Raja and P. Ratnasamy, *Journal of Catalysis*, 1997, **170**, 244-253.

28. E. P. Iaia, G. R. Rana, A. Soyemi, A. B. Shrestha, M. E. S. Martin, J. L. Groeber, C. R. Diemer, T. Szilvási, M. G. Bakker and J. W. Harris, *ACS Applied Nano Materials*, 2024, **7**, 18824-18840.
29. W. Zhu, S. Ndayiragije, X. Zuo, X. Zhang, G. Wang and X. Wang, *Journal of Environmental Chemical Engineering*, 2022, **10**, 107758.
30. C. A. Whitcomb, A. Sviripa, M. I. Schapowal, K. Mamedov, R. R. Unocic, C. Paolucci and R. J. Davis, *ACS Catalysis*, 2022, **12**, 15529-15540.
31. J. W. Harris, M. J. Cordon, J. R. Di Iorio, J. C. Vega-Vila, F. H. Ribeiro and R. Gounder, *Journal of Catalysis*, 2016, **335**, 141-154.
32. W. S. Borghard, E. W. Sheppard and H. J. Schoennagel, *Review of Scientific Instruments*, 1991, **62**, 2801-2809.
33. D. P. Law, A. B. Blakeney and R. Tkachuk, *Journal of Near Infrared Spectroscopy*, 1996, **4**, 189-193.
34. P. Kubelka and F. Munk, *Z. Tech. Phys*, 1931, **12**, 259-274.
35. D. Leshchev, M. Rakitin, B. Luvizotto, R. Kadyrov, B. Ravel, K. Attenkofer and E. Stavitski, *Journal of Synchrotron Radiation*, 2022, **29**, 1095-1106.
36. B. Ravel and M. Newville, *Journal of Synchrotron Radiation*, 2005, **12**, 537-541.
37. A. Jain, S. P. Ong, G. Hautier, W. Chen, W. D. Richards, S. Dacek, S. Cholia, D. Gunter, D. Skinner, G. Ceder and K. A. Persson, *APL Materials*, 2013, **1**, 011002.
38. B. Modén, B.-Z. Zhan, J. Dakka, J. G. Santiesteban and E. Iglesia, *Journal of Catalysis*, 2006, **239**, 390-401.
39. A. Pokutsa, Y. Kubaj, A. Zaborovskyi, D. Maksym, T. Paczesniak, B. Mysliwiec, E. Bidzinska, J. Muzart and A. Sobkowiak, *Molecular Catalysis*, 2017, **434**, 194-205.
40. W. Czerwiński and E. Kurek, *Journal of Chromatography A*, 1984, **286**, 275-278.
41. J. P. Perdew, K. Burke and M. Ernzerhof, *Physical Review Letters*, 1996, **77**, 3865-3868.
42. F. Weigend and R. Ahlrichs, *Physical Chemistry Chemical Physics*, 2005, **7**, 3297-3305.
43. S. Grimme, S. Ehrlich and L. Goerigk, *Journal of Computational Chemistry*, 2011, **32**, 1456-1465.
44. M. J. Frisch, G. W. Trucks, H. B. Schlegel, G. E. Scuseria, M. A. Robb, J. R. Cheeseman, G. Scalmani, V. Barone, G. A. Petersson, H. Nakatsuji, X. Li, M. Caricato, A. V. Marenich, J. Bloino, B. G. Janesko, R. Gomperts, B. Mennucci, H. P. Hratchian, J. V. Ortiz, A. F. Izmaylov, J. L. Sonnenberg, Williams, F. Ding, F. Lipparini, F. Egidi, J. Goings, B. Peng, A. Petrone, T. Henderson, D. Ranasinghe, V. G. Zakrzewski, J. Gao, N. Rega, G. Zheng, W. Liang, M. Hada, M. Ehara, K. Toyota, R. Fukuda, J. Hasegawa, M. Ishida, T. Nakajima, Y. Honda, O. Kitao, H. Nakai, T. Vreven, K. Throssell, J. A. Montgomery Jr., J. E. Peralta, F. Ogliaro, M. J. Bearpark, J. J. Heyd, E. N. Brothers, K. N. Kudin, V. N. Staroverov, T. A. Keith, R. Kobayashi, J. Normand, K. Raghavachari, A. P. Rendell, J. C. Burant, S. S. Iyengar, J. Tomasi, M. Cossi, J. M. Millam, M. Klene, C. Adamo, R. Cammi, J. W. Ochterski, R. L. Martin, K. Morokuma, O. Farkas, J. B. Foresman and D. J. Fox, *Journal*, 2016.
45. A. V. Marenich, C. J. Cramer and D. G. Truhlar, *The Journal of Physical Chemistry B*, 2009, **113**, 6378-6396.
46. R. F. Ribeiro, A. V. Marenich, C. J. Cramer and D. G. Truhlar, *The Journal of Physical Chemistry B*, 2011, **115**, 14556-14562.
47. G. Luchini, J. Alegre-Requena, I. Funes-Ardoiz and R. Paton, *F1000Research*, 2020, **9**.

48. R. W. Ashcraft, S. Raman and W. H. Green, *The Journal of Physical Chemistry B*, 2007, **111**, 11968-11983.
49. Z. Benedek, M. Papp, J. Oláh and T. Szilvási, *ACS Catalysis*, 2020, **10**, 12555-12568.
50. Z. Benedek, M. Papp, J. Oláh and T. Szilvási, *Inorganic Chemistry*, 2019, **58**, 7969-7977.
51. Z. Benedek, M. Papp, J. Oláh and T. Szilvási, *Inorganic Chemistry*, 2018, **57**, 8499-8508.
52. H. Ryu, J. Park, H. K. Kim, J. Y. Park, S.-T. Kim and M.-H. Baik, *Organometallics*, 2018, **37**, 3228-3239.
53. G. Sciortino and F. Maseras, *Theoretical Chemistry Accounts*, 2023, **142**, 99.
54. M. von Smoluchowski, *Annalen der Physik*, 1906, **326**, 756-780.
55. M. Besora and F. Maseras, *WIREs Computational Molecular Science*, 2018, **8**, e1372.
56. P. S. Nikam, L. N. Shirsat and M. Hasan, *Journal of Chemical & Engineering Data*, 1998, **43**, 732-737.
57. G. Gupta and B. C. Bukowski, *The Journal of Physical Chemistry C*, 2024, **128**, 20104-20117.
58. B. C. Bukowski, J. S. Bates, R. Gounder and J. Greeley, *Journal of Catalysis*, 2018, **365**, 261-276.
59. J. S. Bates, B. C. Bukowski, J. W. Harris, J. Greeley and R. Gounder, *ACS Catalysis*, 2019, **9**, 6146-6168.
60. S. Hoops, S. Sahle, R. Gauges, C. Lee, J. Pahle, N. Simus, M. Singhal, L. Xu, P. Mendes and U. Kummer, *Bioinformatics*, 2006, **22**, 3067-3074.
61. C. T. Campbell, *ACS Catalysis*, 2017, **7**, 2770-2779.
62. J. W. M. Osterrieth, J. Rampersad, D. Madden, N. Rampal, L. Skoric, B. Connolly, M. D. Allendorf, V. Stavila, J. L. Snider, R. Ameloot, J. Marreiros, C. Ania, D. Azevedo, E. Vilarrasa-Garcia, B. F. Santos, X.-H. Bu, Z. Chang, H. Bunzen, N. R. Champness, S. L. Griffin, B. Chen, R.-B. Lin, B. Coasne, S. Cohen, J. C. Moreton, Y. J. Colón, L. Chen, R. Clowes, F.-X. Coudert, Y. Cui, B. Hou, D. M. D'Alessandro, P. W. Doheny, M. Dincă, C. Sun, C. Doonan, M. T. Huxley, J. D. Evans, P. Falcaro, R. Ricco, O. Farha, K. B. Idrees, T. Islamoglu, P. Feng, H. Yang, R. S. Forgan, D. Bara, S. Furukawa, E. Sanchez, J. Gascon, S. Telalović, S. K. Ghosh, S. Mukherjee, M. R. Hill, M. M. Sadiq, P. Horcajada, P. Salcedo-Abraira, K. Kaneko, R. Kukobat, J. Kenvin, S. Keskin, S. Kitagawa, K.-i. Otake, R. P. Lively, S. J. A. DeWitt, P. Llewellyn, B. V. Lotsch, S. T. Emmerling, A. M. Pütz, C. Martí-Gastaldo, N. M. Padial, J. García-Martínez, N. Linares, D. Maspoch, J. A. Suárez del Pino, P. Moghadam, R. Oktavian, R. E. Morris, P. S. Wheatley, J. Navarro, C. Petit, D. Danaci, M. J. Rosseinsky, A. P. Katsoulidis, M. Schröder, X. Han, S. Yang, C. Serre, G. Mouchaham, D. S. Sholl, R. Thyagarajan, D. Siderius, R. Q. Snurr, R. B. Goncalves, S. Telfer, S. J. Lee, V. P. Ting, J. L. Rowlandson, T. Uemura, T. Iiyuka, M. A. van der Veen, D. Rega, V. Van Speybroeck, S. M. J. Rogge, A. Lamaire, K. S. Walton, L. W. Bingel, S. Wuttke, J. Andreo, O. Yaghi, B. Zhang, C. T. Yavuz, T. S. Nguyen, F. Zamora, C. Montoro, H. Zhou, A. Kirchon and D. Fairen-Jimenez, *Advanced Materials*, 2022, **34**, 2201502.
63. H. Zhou, Y. Shi, L. Dai, D. Liu and W. Du, *Chemical Engineering Journal*, 2023, **473**, 145218.
64. R. Giovannetti, *Macro to nano spectroscopy*, 2012, 87-108.
65. T. E. Gorelik, S. Habermehl, A. A. Shubin, T. Gruene, K. Yoshida, P. Oleynikov, U. Kaiser and M. U. Schmidt, *Journal*, 2021, DOI: 10.5517/CCDC.CSD.CC27V4R0.
66. J. F. Kirner, W. Dow and W. R. Scheidt, *Journal*, 1976, DOI: 10.1021/ic50161a042.

67. H. Jiang, J. Ye, P. Hu, F. Wei, K. Du, N. Wang, T. Ba, S. Feng and C. Kloc, *Journal*, 2015, DOI: 10.5517/cc1308lz.
68. B. Taylor, J. Lauterbach, G. E. Blau and W. N. Delgass, *Journal of Catalysis*, 2006, **242**, 142-152.
69. V. Mahdavi and H. R. Hasheminasab, *Journal of the Taiwan Institute of Chemical Engineers*, 2015, **51**, 53-62.
70. I. Rekkab-Hammoumraoui and A. Choukchou-Braham, *Bull. Chem. React. Eng. Catal.*, 2018, **13**, 24-35.
71. J.-A. Becerra, L.-M. González and A.-L. Villa, *Journal of Molecular Catalysis A: Chemical*, 2016, **423**, 12-21.
72. S. Li, S. Ali, Z. Zuhra, H. Shen, J. Qiu, Y. Zeng, K. Zheng, X. Wang, G. Xie and S. Ding, *Molecules*, 2024, **29**.
73. S. Ernst and M. Selle, *Microporous and Mesoporous Materials*, 1999, **27**, 355-363.
74. K. J. Balkus, A. Khanmamedova and M. Eissa, *Studies in Surface Science and Catalysis*, 1995, **97**, 189-195.
75. S. Seelan, M. S. Agashe, D. Srinivas and S. Sivasanker, *Journal of Molecular Catalysis A: Chemical*, 2001, **168**, 61-68.
76. N. Sehlotho and T. Nyokong, *Journal of Molecular Catalysis A: Chemical*, 2004, **209**, 51-57.
77. Z. Bıyıklıoğlu, E. T. Saka, S. Gökçe and H. Kantekin, *Journal of Molecular Catalysis A: Chemical*, 2013, **378**, 156-163.
78. N. Grootboom and T. Nyokong, *Journal of Molecular Catalysis A: Chemical*, 2002, **179**, 113-123.
79. D. H. R. Barton and D. Doller, *Accounts of Chemical Research*, 1992, **25**, 504-512.
80. O. L. Kaliya, E. A. Lukyanets and G. N. Vorozhtsov, *Journal of Porphyrins and Phthalocyanines*, 1999, **3**, 592-610.
81. A. Ebadi and F. Nikbakht, *Reaction Kinetics, Mechanisms and Catalysis Reac Kinet Mech Cat*, 2011, **104**, 37-47.

The data supporting this article have been included as part of the Supplementary Information.